The Astrophysical Journal Supplement Series, 283:6 (28pp), 2026 March https://doi.org/10.3847/1538-4365/ae3163

Overview of the JWST Advanced Deep Extragalactic Survey (JADES)

Daniel J. Eisenstein[1], Chris Willott[2], Stacey Alberts[3], Santiago Arribas[4], Nina Bonaventura[3,5,6], Andrew J. Bunker[7], Alex J. Cameron[7], Stefano Carniani[8], Stephane Charlot[9], Emma Curtis-Lake[10], Francesco D'Eugenio[11,12], Pierre Ferruit[13], Giovanna Giardino[14], Kevin Hainline[3], Ryan Hausen[15], Peter Jakobsen[5,6], Benjamin D. Johnson[1], Roberto Maiolino[11,12,16], Bernard J. Rauscher[17], Marcia Rieke[3], George Rieke[18], Hans-Walter Rix[19], Brant Robertson[20], Daniel P. Stark[3], Sandro Tacchella[11,12], Christina C. Williams[21], Christopher N. A. Willmer[3], William M. Baker[11,12], Stefi Baum[22], Rachana Bhatawdekar[23,24], Kristan Boyett[25,26], Zuyi Chen[3], Jacopo Chevallard[7], Chiara Circosta[23], Mirko Curti[11,12,27], A. Lola Danhaive[11], Christa DeCoursey[3], Ryan Endsley[28], Anna de Graaff[19], Alan Dressler[29], Eiichi Egami[3], Jakob M. Helton[3], Raphael E. Hviding[3], Zhiyuan Ji[3], Gareth C. Jones[7], Nimisha Kumari[30], Nora Lützgendorf[31], Isaac Laseter[32], Tobias J. Looser[11], Jianwei Lyu[3], Michael V. Maseda[32], Erica Nelson[33], Eleonora Parlanti[8], Michele Perna[4], Dávid Puskás[11,12], Tim Rawle[34], Bruno Rodríguez Del Pino[4], Wiphu Rujopakarn[35,36], Lester Sandles[11,12], Aayush Saxena[7,16], Jan Scholtz[11,12], Katherine Sharpe[1], Irene Shivaei[3], Maddie S. Silcock[10], Charlotte Simmonds[11,12], Maya Skarbinski[1,37], Renske Smit[38], Meredith Stone[3], Katherine A. Suess[20,39], Fengwu Sun[3], Mengtao Tang[3], Michael W. Topping[3], Hannah Übler[11,12], Natalia C. Villanueva[1], Imaan E. B. Wallace[7], Lily Whitler[3], Joris Witstok[11,12], and Charity Woodrum[3]

[1] Center for Astrophysics | Harvard & Smithsonian, 60 Garden Street, Cambridge MA 02138, USA
[2] NRC Herzberg, 5071 West Saanich Road, Victoria, BC V9E 2E7, Canada
[3] Steward Observatory, University of Arizona, 933 N. Cherry Avenue, Tucson, AZ 85721, USA
[4] Centro de Astrobiología (CAB), CSIC-INTA, Cra. de Ajalvir Km. 4, 28850-Torrejón de Ardoz, Madrid, Spain
[5] Cosmic Dawn Center (DAWN), Copenhagen, Denmark
[6] Niels Bohr Institute, University of Copenhagen, Jagtvej 128, DK-2200, Copenhagen, Denmark
[7] Department of Physics, University of Oxford, Denys Wilkinson Building, Keble Road, Oxford OX1 3RH, UK
[8] Scuola Normale Superiore, Piazza dei Cavalieri 7, I-56126 Pisa, Italy
[9] Sorbonne Université, CNRS, UMR 7095, Institut d'Astrophysique de Paris, 98 bis bd Arago, 75014, Paris, France
[10] Centre for Astrophysics Research, Department of Physics, Astronomy and Mathematics, University of Hertfordshire, Hatfield AL10 9AB, UK
[11] Kavli Institute for Cosmology, University of Cambridge, Madingley Road, Cambridge CB3 0HA, UK
[12] Cavendish Laboratory, University of Cambridge, 19 JJ Thomson Avenue, Cambridge CB3 0HE, UK
[13] European Space Agency, European Space Astronomy Centre, Camino Bajo del Castillo s/n, 28692, Villafranca del Castillo, Madrid, Spain
[14] ATG Europe for the European Space Agency, ESTEC, Noordwijk, The Netherlands
[15] Department of Physics and Astronomy, The Johns Hopkins University, 3400 N. Charles Street, Baltimore, MD 21218, USA
[16] Department of Physics and Astronomy, University College London, Gower Street, London WC1E 6BT, UK
[17] Observational Cosmology Laboratory, NASA Goddard Space Flight Center, 8800 Greenbelt Road, Greenbelt, MD 20771, USA
[18] Steward Observatory and Dept. of Planetary Sciences, University of Arizona, 933 N. Cherry Avenue, Tucson, AZ 85721, USA
[19] Max-Planck-Institut für Astronomie, Königstuhl 17, D-69117, Heidelberg, Germany
[20] Department of Astronomy and Astrophysics University of California, Santa Cruz, 1156 High Street, Santa Cruz, CA 96054, USA
[21] NSF's National Optical-Infrared Astronomy Research Laboratory, 950 N. Cherry Avenue, Tucson, AZ 85719, USA
[22] Department of Physics and Astronomy, University of Manitoba, Winnipeg, MB R3T 2N2, Canada
[23] European Space Agency (ESA), European Space Astronomy Centre (ESAC), Camino Bajo del Castillo s/n, 28692, Villanueva de la Cañada, Madrid, Spain
[24] European Space Agency, ESA/ESTEC, Keplerlaan 1, 2201 AZ Noordwijk, The Netherlands
[25] School of Physics, University of Melbourne, Parkville 3010, VIC, Australia
[26] ARC Centre of Excellence for All Sky Astrophysics in 3 Dimensions (ASTRO 3D), Australia
[27] European Southern Observatory, Karl-Schwarzschild-Strasse 2, 85748 Garching, Germany
[28] Department of Astronomy, University of Texas, Austin, TX 78712, USA
[29] The Observatories of the Carnegie Institution for Science, 813 Santa Barbara Street, Pasadena, CA 91101, USA
[30] AURA for European Space Agency, Space Telescope Science Institute, 3700 San Martin Drive, Baltimore, MD 21210, USA
[31] European Space Agency, Space Telescope Science Institute, Baltimore, MD, USA
[32] Department of Astronomy, University of Wisconsin-Madison, 475 N. Charter Street, Madison, WI 53706, USA
[33] Department for Astrophysical and Planetary Science, University of Colorado, Boulder, CO 80309, USA
[34] European Space Agency (ESA), European Space Astronomy Centre (ESAC), Camino Bajo del Castillo s/n, 28692, Villafranca del Castillo, Madrid, Spain
[35] National Astronomical Research Institute of Thailand, Don Kaeo, Mae Rim, Chiang Mai 50180, Thailand
[36] Department of Physics, Faculty of Science, Chulalongkorn University, 254 Phayathai Road, Pathumwan, Bangkok 10330, Thailand
[37] William H. Miller III Department of Physics and Astronomy, Johns Hopkins University, Baltimore, MD 21218, USA
[38] Astrophysics Research Institute, Liverpool John Moores University, 146 Brownlow Hill, Liverpool L3 5RF, UK
[39] Kavli Institute for Particle Astrophysics and Cosmology and Department of Physics, Stanford University, Stanford, CA 94305, USA

Received 2023 June 4; revised 2025 December 6; accepted 2025 December 17; published 2026 February 11

Abstract

We present an overview of the James Webb Space Telescope (JWST) Advanced Deep Extragalactic Survey (JADES), an ambitious program of infrared imaging and spectroscopy in the GOODS-S and GOODS-N deep fields, designed to study galaxy evolution from high redshift to cosmic noon. JADES uses about 770 hr of Cycle 1 guaranteed time largely from the Near-Infrared Camera (NIRCam) and Near-Infrared Spectrograph (NIRSpec) instrument teams. In GOODS-S, in and around the Hubble Ultra Deep Field and Chandra Deep Field South, JADES produces a deep imaging region of $\sim$42 arcmin^2 with over 100 hr of exposure time spread over nine NIRCam filters, including two medium-band filters. This is extended at medium depth in GOODS-S and GOODS-N with NIRCam imaging of $\sim$167 arcmin^2, averaging 25 hr of exposure over 8–10 filters. In both fields, we conduct extensive NIRSpec multiobject spectroscopy, including two deep pointings of 55 hr exposure time, 14 medium pointings of $\sim$12 hr, and 15 shallower pointings of $\sim$4 hr, targeting over 5000 Hubble Space Telescope– and JWST-detected faint sources with five low-, medium-, and high-resolution dispersers covering 0.6–5.3 μm. Finally, JADES extends redward via coordinated parallels with the JWST Mid-Infrared Instrument, featuring $\sim$10 arcmin^2 with 43 hr of exposure at 7.7 μm and thrice that area with 1.4–6.8 hr of exposure at 12.8 and 15 μm. For nearly 30 yr, the GOODS-S and GOODS-N fields have been developed as the premier deep fields on the sky; JADES is now providing a compelling start on JWST's legacy in these fields.

Unified Astronomy Thesaurus concepts: Sky surveys (1464); Galaxy evolution (594); Lyman-break galaxies (979)

1. Introduction

The James Webb Space Telescope (JWST) is revolutionizing the study of galaxy evolution by providing us with unprecedented access to deep, sharp, and nuanced infrared imaging and spectroscopy. Designed to push the redshift frontier and bring the early growth of galaxies into clear focus, the telescope is performing at, or even better than, expectations (J. Rigby et al. 2023). JWST takes marvelous advantage of the faintness of the zodiacal foregrounds at 2–10 μm and state-of-the-art infrared detectors to unlock the rest-frame optical at redshifts $z > 4$, combining large collecting area and diffraction-limited imaging. Exploiting this telescope are ambitious multipurpose instruments (J. P. Gardner et al. 2023) that give us dozens of selectable filters, exquisite slitless, integral-field or multiobject spectroscopy (MOS) and multiple coronagraphs.

Unraveling the physics of high-redshift galaxies will require the combination of many different kinds of observations. While there are important observations of rare, extreme phenomena, many goals in studying the general population are well served by deep-sky general surveys, as each image contains an unbiased superposition of all epochs of galaxy evolution. Of course, low redshifts are best served by wider, shallower data, but great depth is required to identify and characterize high-redshift galaxies.

The Hubble Deep Field was a dramatic advance in this regard. It boldly unveiled the high-redshift Universe in a single multicolor blank-field image (R. E. Williams et al. 1996; H. C. Ferguson et al. 2000). Since then, such surveys have been vigorously pursued, utilizing virtually every high-sensitivity narrow-field telescope. This field and that of the Chandra Deep Field South (R. Giacconi et al. 2002) were broadened out to form the Great Observatories Origins Deep Survey (GOODS; M. Giavalisco et al. 2004), utilizing the new opportunities of the Hubble Space Telescope (HST) Advanced Camera for Surveys (ACS) and Spitzer infrared telescope to partner with deep Chandra X-ray imaging (B. Luo et al. 2008). Soon after, the Hubble Ultra Deep Field (HUDF) was sited in the heart of GOODS-S (S. V. W. Beckwith et al. 2006). It has since become the standard bearer of deep fields, pushing into the Epoch of Reionization by leveraging exceptional optical and infrared HST imaging, e.g., the UDF09 (R. J. Bouwens et al. 2010) and UDF12 programs (R. S. Ellis et al. 2013), with tremendous investments across the electromagnetic spectrum from many other imaging and spectroscopic facilities.

JWST is designed to pursue such surveys; the telescope provides exquisite image quality and depth, but it moves slowly enough that deep fields are operationally favored. Every pointing of practical depth reveals tens of thousands of galaxies, including many at $z > 6$ where the intergalactic medium (IGM) completely blocks optical light. Further, JWST provides a novel opportunity to conduct detailed faint multi-object spectroscopy beyond 2 μm, where critical rest-optical lines are shifted at high redshift. Numerous projects have already started this work, which we expect will be one of the enduring legacies of the telescope (B. E. Robertson 2022).

Here, we describe the JWST Advanced Deep Extragalactic Survey (JADES), a collaboration of the Near-Infrared Camera (NIRCam) and Near-Infrared Spectrograph (NIRSpec) Instrument Development Teams. The plans to conduct deep-field imaging and spectroscopy were featured in the original instrument proposals, with the intent to devote a substantial amount of guaranteed time to this topic. In 2015, the teams joined to form a larger and more coordinated project, now called JADES, to focus on the exceptional opportunities of JWST onto the GOODS-S and GOODS-N fields. In doing so, it became possible to carry out a project with fewer compromises: deep and wide enough to support the geometry of the instrument footprints and utilize efficient parallel observations, with robust well-dithered imaging and spectroscopy in many filters and several dispersion modes.

At about 770 hr of observing time plus coordinated parallels, JADES is the largest program operating in JWST Cycle 1 and is a very large investment of instrument team guaranteed time. The time was roughly evenly split between the NIRCam and NIRSpec GTO budgets, with a supplementary contribution from the MIRI-US team. By applying the experience of the teams that designed and commissioned the instruments, we aim to provide an exquisite legacy dataset for these deep fields.

In this overview paper, we describe the scientific motivations and resulting survey design of JADES, providing an overview of how we developed our strategy to maximize performance in both imaging and spectroscopy in the targeted fields. Descriptions of the data reduction and spectroscopic

target selection are being presented in the data release papers (D. J. Eisenstein et al. 2023; M. J. Rieke et al. 2023b; A. J. Bunker et al. 2024; F. D'Eugenio et al. 2025; E. Curtis-Lake et al. 2026, in preparation; J. Scholtz et al. 2026, in preparation).

2. JADES Science Goals

2.1. Motivations

The sensitivity and instrumentation of JWST provide a singular opportunity to study the evolution of galaxies from the earliest epochs $\lesssim$300 Myr after the Big Bang, through the Epoch of Reionization during the first billion years of cosmic history, and on to Cosmic High Noon where the stellar mass and black hole mass densities of the Universe were well established. Unlike all other previous studies of high-redshift (i.e., $z > 3$) galaxy populations where only rest-frame ultraviolet spectral properties have been accessible, JWST enables for the first time, via its instruments NIRCam (M. J. Rieke et al. 2023a), NIRSpec (P. Ferruit et al. 2022; P. Jakobsen et al. 2022), NIRISS (R. Doyon et al. 2023), and MIRI (G. S. Wright et al. 2023), photometry and spectroscopy extending from blueward of the Lyman break to redward of the Balmer/4000 Å break region. In this section, we describe how our view of the Universe before the launch of JWST shaped the design of JADES and how early JWST observations support our decisions.

At the earliest times in cosmic history (e.g., <500 Myr), the first abundant population of star-forming galaxies developed. Galaxy formation is a self-regulated process, and the ways in which early galaxies respond to the rapid accretion and cooling of gas greatly affects their bulk properties like luminosity and size. Through perseverance in HST imaging surveys, a handful of galaxies at $z \sim 10$–11 were discovered (D. Coe et al. 2013; P. A. Oesch et al. 2016), enabling a first glance at the primitive galaxy formation process.

JWST has the sensitivity and the required array of infrared filters to identify galaxies selected in rest-frame ultraviolet (UV) at $z > 12$, farther than any tentative HST detections. Hundreds of hours of NIRCam multifilter imaging yields sufficient source counts to measure the UV luminosity function evolution out to $z \sim 10$ and beyond. JADES includes medium-band filters in the NIRCam long-wave channel that can help identify and distinguish high-z candidates from dusty, strong emission-line sources at lower redshifts (e.g., P. Arrabal Haro et al. 2023; S. Fujimoto et al. 2023; J. A. Zavala et al. 2023). The most distant galaxies are inevitably very faint and these NIRCam discoveries require very long integrations with the NIRSpec low-resolution prism for redshift confirmation, especially at redshifts $z > 10$ where the strongest optical lines are redshifted beyond the NIRSpec range (E. Curtis-Lake et al. 2023; B. E. Robertson et al. 2023a).

Extending redder than Hubble and reaching many magnitudes deeper than ever achieved with Spitzer, JWST greatly improves our census of the early Universe, tracing the growth of galaxies at this early epoch. Combining the SFR and stellar masses derived from spectral energy distributions (SEDs) spanning the rest-UV and optical, NIRCam and MIRI imaging allow estimates of the stellar birth rate of galaxies out to $z \sim 10$ to deliver our earliest constraints on the efficiency of galaxy formation (e.g., R. Endsley et al. 2023; I. Labbé et al. 2023; S. Tacchella et al. 2023). Stellar masses measured at $z \sim 10$ allow us to infer a bulk star formation rate to $z \gtrsim 12$ (given the minimum $\sim$100 Myr timescale typically required for the development of strong rest-frame optical breaks; A. Dressler et al. 2023; L. Whitler et al. 2023). Rest-UV emission lines, such as [C IV](1549 Å), He II(1640 Å), O III](1663 Å), and C III](1909 Å), are accessible to NIRSpec to the highest redshifts to measure the physical properties of nebular gas and infer their sources of ionization (A. J. Bunker et al. 2023; M. Tang et al. 2023; T. Y.-Y. Hsiao et al. 2024). Our window into early galaxies with JWST becomes dramatically richer at just slightly later times ($z \sim 8$–9) where NIRSpec can measure the rest-frame optical strong lines (e.g., [O II], [Ne III], Hβ, [O III], and even Hα at $z < 7$) and both the Lyman and Balmer/4000 Å breaks (A. J. Cameron et al. 2023; N. A. Reddy et al. 2023a; R. L. Sanders et al. 2023; M. Tang et al. 2023). NIRCam imaging in medium and wide filters can measure these breaks and strong lines, and given enough filters can differentiate between the two (R. Endsley et al. 2023; C. C. Williams et al. 2023; S. Withers et al. 2023).

From previous surveys of the cosmic microwave background, quasars, and galaxies, we know that these epochs experience the first important contributions of galaxies to the cosmic reionization process (Planck Collaboration et al. 2020; B. E. Robertson 2022; X. Fan et al. 2023). Here, JWST simultaneously constrains the evolving rest-frame UV galaxy luminosity density and provides information on the hardness of the ionizing continuum and the escape fraction of Lyman continuum photons (R. Bouwens et al. 2023; C. T. Donnan et al. 2023; R. Endsley et al. 2023; S. Mascia et al. 2023; C. Simmonds et al. 2023). These measurements result in a more accurate "balancing of the budget" for cosmic reionization, where we weigh the cosmic ionization rate against the recombination of the intergalactic hydrogen in determining the evolving bulk IGM neutrality. Mapping with spectra the "Lyα disappearance," measuring the evolving fraction of UV-dropout selected galaxies that show (or not) Lyα emission, can track how the increased IGM neutrality at earlier times extinguishes observed line emission in progressively more of the sources (A. Fontana et al. 2010; D. P. Stark et al. 2010; L. Pentericci et al. 2014; C. A. Mason et al. 2018; M. Ouchi et al. 2020; G. C. Jones et al. 2024). Correlating the transmission of Lyα with photometric or spectroscopic measurements of environment provides further insight into the topology of ionized bubbles during this epoch (M. Tang et al. 2023; R. Endsley et al. 2024; I. Jung et al. 2024; T.-Y. Lu et al. 2024; L. Whitler et al. 2024; J. Witstok et al. 2024).

Rest-frame optical line spectroscopy at $z \sim 6$–9 dramatically extends our knowledge of the chemical enrichment of galaxies and reveals the physical conditions in the warm interstellar medium (ISM) of early star-forming galaxies. Line excitation diagrams provide insights into the ionization state of the star-forming ISM in these systems; NIRSpec allows us to apply these diagnostics in an entirely new redshift regime (e.g., A. J. Cameron et al. 2023; N. A. Reddy et al. 2023a; R. L. Sanders et al. 2023), connecting them with the properties of the exciting stellar populations. Via the combined measures of star formation rate in the rest-UV, stellar mass in the rest-optical, and metallicity from nebular lines, we can explore whether the fundamental metallicity and mass–metallicity relations are already in place after only $\sim$1 Gyr of cosmic history (M. Curti et al. 2023; K. Nakajima et al. 2023).

JWST is revealing the emergence of morphological structures at $z > 2$ through superb infrared imaging

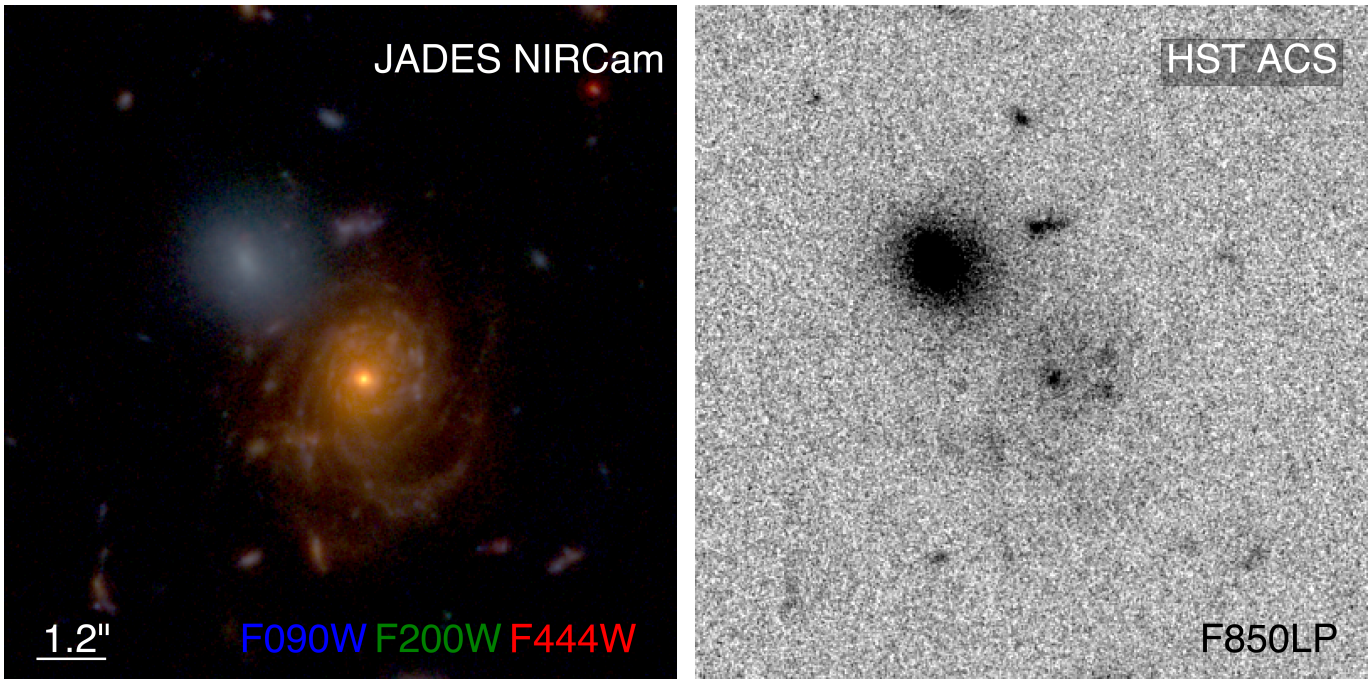

Figure 1. A grand design spiral at redshift 2 revealed in JADES imaging in GOODS-S. Left panel: the JWST NIRCam image combining F090W, F200W, and F444W filters in the Deep Prime region of program 1180. Right panel: the Hubble Space Telescope (HST) Advanced Camera for Surveys (ACS) F850LP image (G. Illingworth et al. 2016; K. E. Whitaker et al. 2019), where this star-forming galaxy is all but invisible. While JADES F090W imaging is deeper than the HST F850LP data here, this image shows the essential value of observing at redder wavelengths.

(L. Ferreira et al. 2022, 2023; C. Jacobs et al. 2023; J. S. Kartaltepe et al. 2023; B. Magnelli et al. 2023; B. E. Robertson et al. 2023b; M. Huertas-Company et al. 2024; W. M. Baker et al. 2025). JWST can resolve these galaxies from the rest-UV to the rest-optical, providing spatially resolved measures of color gradients and stellar population properties, vastly outperforming HST (e.g., Figure 1). We can distinguish the clumpy UV-bright morphology from the rest-optical light on a galaxy-by-galaxy basis, and thereby constrain the role of large-scale gravitational instability in setting galaxy structures at $z \sim 2$–3. NIRSpec spectroscopy with the medium- or high-resolution gratings connects these morphological measures to the dynamics of the galaxies, and through measuring outflows, further constrains the role of feedback in shaping these maturing galaxies.

HST has found compact red galaxies at $z = 2$, but JWST's angular resolution, sensitivity, and redder bands are proving revolutionary to explore old stellar populations and their morphology at $z > 3$ (K. A. Suess et al. 2022; A. C. Carnall et al. 2023; Z. Ji et al. 2024). With NIRCam imaging, including medium filters, Balmer and D_{4000} breaks can be cleanly picked out. Spectroscopy at $R = 100$ with the NIRSpec prism provides precise redshifts and break strengths, but higher-resolution spectroscopy enables more detailed constraints on star formation history (SFH) and abundances at $z > 3$–4, an era that prior to JWST was prohibitive or impossible to study, but critical to our understanding of why and how galaxies stop forming stars (A. C. Carnall et al. 2023; T. Nanayakkara et al. 2024). The importance of burstiness in the evolution of galaxies is now becoming clear with several examples of $z > 5$ galaxies undergoing "mini-quenching" episodes (V. Strait et al. 2023; T. J. Looser et al. 2024). Additional evidence for burstiness is now becoming apparent in statistical samples of NIRCam SEDs (A. Dressler et al. 2023; R. Endsley et al. 2024).

Dust attenuation and reddening in the rest-frame UV and optical spectra and SEDs of galaxies strongly affect the inferred physical quantities, so it is important to study the underlying dust properties. JWST opens a new window to identify and characterize obscured populations that were completely missed by even the deepest Spitzer and HST surveys. The Atacama Millimeter/submillimeter Array (ALMA) has revealed that such hidden galaxies likely contribute significantly to the cosmic star formation rate density at $3 < z < 8$ (e.g., C. C. Williams et al. 2019; Y. Fudamoto et al. 2021; H. S. B. Algera et al. 2023), and early JWST data is supporting this finding (L. Barrufet et al. 2023). The stellar SEDs and morphologies of dust-obscured galaxies at $z > 3$ can now be characterized in detail for the first time (C. Gómez-Guijarro et al. 2023; E. J. Nelson et al. 2023; P. G. Pérez-González et al. 2023). JWST is indicating that massive galaxies have nonnegligible dust content at high redshift, pointing to efficient production mechanisms even out to $z \sim 8$ (H. B. Akins et al. 2023; J. McKinney et al. 2023). The combination of multiband NIRCam photometry and multiline NIRSpec spectroscopy offers the opportunity to tackle these issues through SED-fitting and through line diagnostics such as the Paschen and Balmer decrements and 2200 Å bump (e.g., N. A. Reddy et al. 2023b; A. E. Shapley et al. 2023; J. Witstok et al. 2023; L. Sandles et al. 2024).

The intimate connection between the growth of galaxies and their supermassive black holes can be traced back to the earliest epochs with deep JWST imaging and spectroscopy. Active galactic nuclei (AGNs) are being discovered via their pointlike morphology (particularly in the redder bands; e.g., L. J. Furtak et al. 2023; I. Labbé et al. 2023), broad wings of Balmer emission lines (e.g., Figure 2, but also from NIRCam

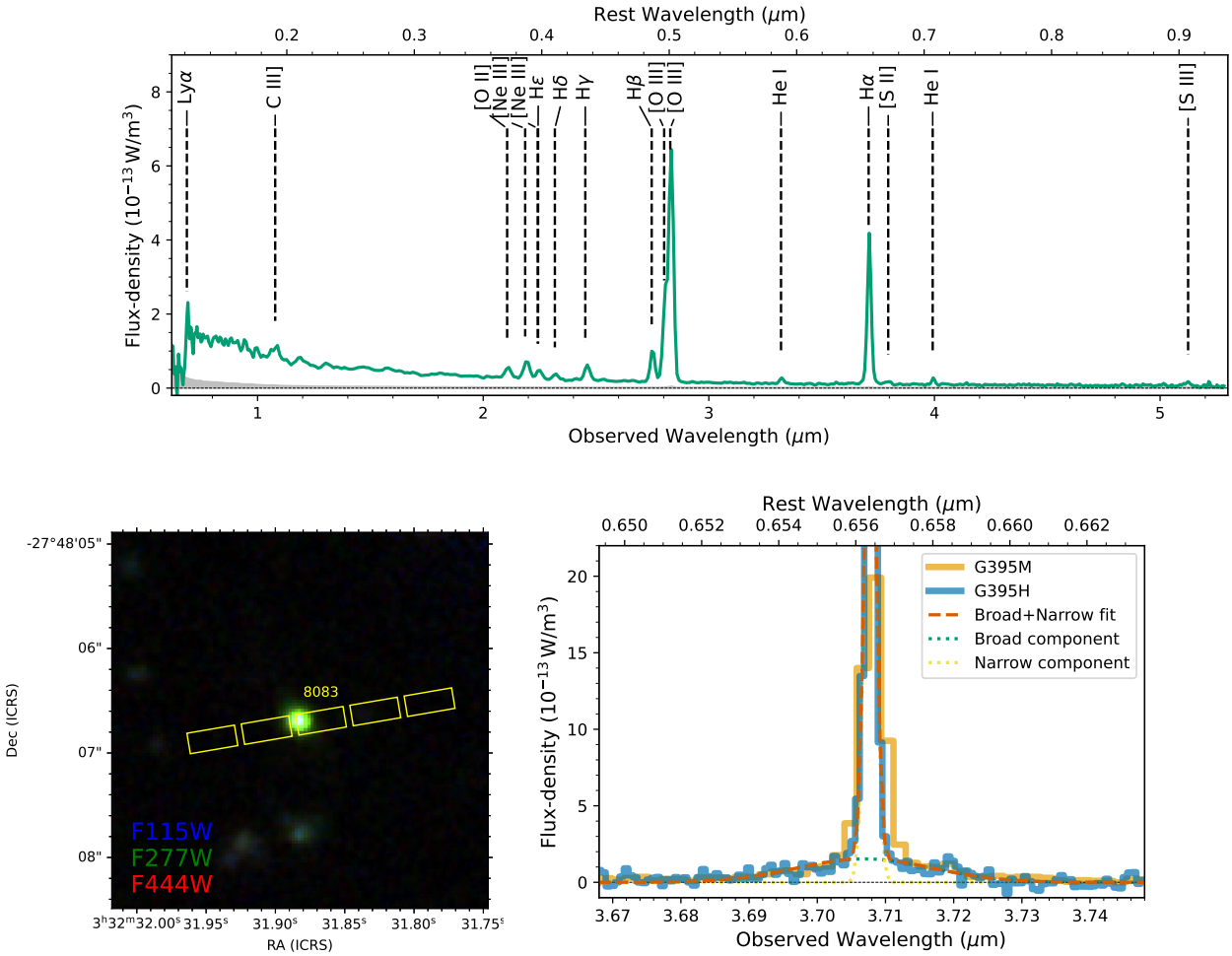

Figure 2. Example spectra for the $z = 4.65$ galaxy JADES-GS+53.13284-27.80185 (ID = 00008083) from the JADES Deep/HST observations. The upper panel shows the low-resolution prism spectrum (total integration time 10^5 s). This spectrum reveals many emission lines and high signal-to-noise ration (S/N) continuum. However, some emission lines are blended or have low equivalent width, motivating the acquisition of grating spectra for most of the galaxies with prism spectra in JADES. The rms uncertainty is shown in the gray shaded spectrum at the bottom of the plot. The lower-left panel shows the JADES Deep imaging data of this galaxy with an overlay of the position of the microshutters during the three nods. The green color of the galaxy indicates [O III] and Hβ line emission dominating in the F277W filter. For the angular scale, we remind the reader that the individual microshutters are 0.″2 by 0.″46. The lower-right panel shows the Hα spectra obtained with the medium G395M and high G395H resolution gratings. Both these spectra reveal a broad ($\sigma = 800$ km s^{-1}) emission line from a low-luminosity AGN broad-line region (R. Maiolino et al. 2024a). However, the G395H grating is required to spectrally resolve the narrow-line emission from the galaxy itself (observed $\sigma = 65$ km s^{-1}, compared to instrumental line spread function $\sigma = 30$ km s^{-1}; A. de Graaff et al. 2024).

grism spectroscopy such as J. Matthee et al. 2024), and highly ionized narrow lines (Y. Harikane et al. 2023; D. D. Kocevski et al. 2023; R. L. Larson et al. 2023; R. Maiolino et al. 2024b; J. Scholtz et al. 2025). In most cases, these AGNs are not detectable even by very deep Chandra or JVLA imaging, putting JWST at the forefront of the quest for the earliest supermassive black holes. With JADES, we obtain deep NIRCam and MIRI imaging plus deep NIRSpec spectroscopy to discover these previously hidden AGNs and investigate the evolving relationship between supermassive black holes and their host galaxies.

Throughout these epochs, the development of the galaxy populations remains tightly connected with the structure formation process in our ΛCDM cosmology Universe. The rates of star formation, stellar population aging, merging, and dynamical and morphological transformation are ultimately manifestations of the growth of dark matter halos. JWST is providing a new context for understanding the connection between galaxy and dark matter structure formation by aiming to discover the earliest galaxies that form in rare peaks of the density field, establishing both the SFR–halo mass and stellar mass–halo mass relations out to $z \sim 10$, watching the emergence of dynamically cold galactic structures, and by observing the assembly of the first massive galaxies that form primarily through dissipationless mergers. The new spectroscopic capabilities allow us to identify physically associated galaxies in the early Universe rather than just projected overdensities (D. Kashino et al. 2023; T. Morishita et al. 2023; J. M. Helton et al. 2024; F. Sun et al. 2024) and enable us to distinguish between how central and satellite galaxies evolve further back in time than has previously been possible. The combination of area and depth allows for clustering analyses down to very faint magnitudes on spectroscopically informed samples with well-constrained redshift selection functions. This combination can also address critical gaps in our knowledge of environmentally driven galaxy evolution. The key epochs of stellar growth and the subsequent quenching in groups and (proto)clusters likely often occur in a dust-obscured phase (see S. Alberts & A. Noble 2022, for a review), necessitating rest-frame near- and mid-infrared

observations that are robust against extinction and directly probe obscured activity. In all, JWST allows for a more physically complete view of galaxy formation that builds directly from the underlying ΛCDM framework.

We stress that most if not all of these science drivers require a substantial survey volume, not just depth. We aim to slice the galaxy samples in a variety of parameters for inter-comparison. Going deep may (slowly) reveal the less-luminous galaxies, but we need to gather sufficient samples of the L^* and brighter ones as well. Rare phases, such as AGN and extreme starbursts, can be important for the evolutionary story. Large-scale structure is prominent even at high redshifts because galaxies are extremely biased tracers of the underlying density field. On the scale of one NIRCam or NIRSpec MOS pointing, this can cause the fluctuations in the number of objects, particularly those from the most-massive halos, to vary substantially (C. L. Steinhardt et al. 2021). Larger surveys allow one to measure more accurate luminosity functions, but also to potentially measure the clustering amplitude itself, which bears on the mass of the host halos as well as on possible Mpc-scale environmental drivers in galaxy evolution.

The above science cases can all be addressed efficiently through a deep extragalactic survey. Typical high-redshift galaxies are common on the sky but very faint. The scientific exploitation of images is necessarily broad simply because of projection of the line of sight, but this is also true for efficient use of multiobject spectroscopy. Since the advent of the Hubble Deep Field, the community has been focusing its resources onto a small number of deep fields, so that the synergies between different types of data can be best exploited. Our survey follows this same logic.

2.2. Opportunities of a Combined Imaging and Spectroscopy Program

As the combination of imaging and spectroscopy is a key driver of our coordinated parallel strategy, we want to stress that JWST imaging and spectroscopy reinforce each other in numerous critical ways.

First, one has the obvious aspect that imaging and spectroscopy constrain different physical properties of the galaxies, which we seek to combine.

Second, having accurate redshifts is important for the interpretation of imaging in terms of luminosities, rest-frame colors, and proper sizes. For example, the conversion of SEDs to stellar masses and SFHs can easily be degenerate with redshift uncertainty. Spectroscopy is the gold standard for redshifts, and JWST has sufficient sensitivity and multiplex to provide spectroscopic redshifts for thousands of galaxies all the way to $z > 10$. Moreover, our program is providing large training samples for the photometric redshift methods that supply redshifts for the rest of the imaging sample.

Third, there are technical synergies. NIRCam broadband filters in the rest-frame optical can have substantial contribution from very strong emission lines, as illustrated by the recent JWST results (A. J. Cameron et al. 2023; J. Matthee et al. 2023). NIRSpec spectroscopy is providing the location and fluxes of these lines, enabling us to subtract them to accurately measure the continuum SED. This is important for the estimation of stellar population age distributions. We can do this subtraction directly in thousands of objects but also measure the trends and variations needed to model the purely photometric samples.

NIRCam, in turn, is important for NIRSpec MOS to understand its slit losses, background subtraction, and to aid in the interpretation of emission-line kinematics. Unlike ground-based slit masks, the NIRSpec microshutter array (MSA) provides a fixed grid of slits. Galaxies fall at various registrations relative to those slits and with a range of sizes. Achieving accurate line-flux calibration requires the imaging to provide a model of this. Further, NIRSpec MOS background subtraction requires the subtraction of neighboring shutters; only NIRCam can provide a deep 2–5 μm probe of contaminating objects in these shutters. Eventually, we expect that the sharp NIRCam images will provide morphological templates for more ambitious extraction of undersampled NIRSpec spectra, going beyond just summing along the spatial direction of a slit.

Fourth, JWST imaging can allow for more efficient target selection for NIRSpec MOS spectroscopy of rare populations. While HST can provide Lyman-dropout selection for UV-bright targets, the longer wavelength coverage of JWST yields much improved photometric redshifts for redder objects. NIRCam medium-band imaging can isolate objects with strong rest-frame optical line emission that can then be targeted for line profile studies with the NIRSpec gratings.

Finally, there are more subtle astrophysical synergies. For strong line emitters, the high signal-to-noise ratio (S/N) and the excellent angular resolution of NIRCam provide, via the comparison of different filters, measurements of size and morphology of the line emission relative to the stellar light. NIRCam imaging can reveal color gradients to be correlated with spectral properties. For spatially extended galaxies, one can even connect these to resolved spectral variations along the slits.

We note that while the combination of imaging and spectroscopy is critically important, it is not the case that one requires spectroscopy for every imaging object. Rather, one intends to use the spectroscopy to build models of the trends, so that one can perform statistical work on the nonspectroscopic sample.

3. JADES Survey Design

3.1. Field Selection

JADES seeks to combine deep multiband imaging and spectroscopy in pursuit of the science goals described in Section 2. It is designed to bring NIRCam and NIRSpec MOS together on a common region of the sky, while covering substantial areas in two different fields in order to increase the statistical reach for rare objects and sample large-scale structure.

We observe two fields in JADES, to avoid concern that the large-scale structure of highly biased tracers and the radiation transport of reionization could make any one field peculiar and limit confidence in any unusual results. Further, we wanted to spread the observing around the year to ease the constraints on scheduling such a large program. Of course, even more fields would better mitigate the concerns about cosmic variance, but this would limit the depth and area of each.

The choice of location was driven by the availability of deep panchromatic imaging and spectroscopy, as the study of galaxy evolution draws on a wide range of such input. This led us clearly to the GOODS-South and GOODS-North fields, which have received huge investments of telescope time over

the past 25 yr from essentially every facility that bears on the high-redshift Universe.

GOODS-South, home of the Chandra Deep Field South and the Hubble Ultra Deep Field as well as very deep ALMA (F. Walter et al. 2016; J. S. Dunlop et al. 2017; M. Franco et al. 2018; B. Hatsukade et al. 2018) and JVLA data (W. Rujopakarn et al. 2016; S. Alberts et al. 2020), is the preeminent deep field on the sky. We chose this as the primary field for JADES and focused the majority of the observing time there. GOODS-North, home of the Hubble Deep Field and exceptionally deep Chandra data, was chosen as the second field.

By placing JADES in the legacy GOODS fields, we seek to augment the rich HST community data products with a comprehensive set of JWST imaging and spectroscopy. The GOODS (M. Giavalisco et al. 2004), CANDELS (N. A. Grogin et al. 2011; A. M. Koekemoer et al. 2011), and UDF (S. V. W. Beckwith et al. 2006; R. S. Ellis et al. 2013; G. D. Illingworth et al. 2013) data have been reduced and released as components of the Hubble Legacy Fields (HLF; G. Illingworth et al. 2016; K. E. Whitaker et al. 2019). The HLF reductions provide an excellent matched set of HST images in multiple ACS and WFC3 bands for use with the JADES JWST NIRCam imaging. We also utilize astrometric registration to Gaia performed by G. Brammer (2025, private communication) using the methods of V. Kokorev et al. (2022) and *grizli* (G. Brammer 2023).

3.2. Tiers and Geometrical Constraints

JADES is built as a two-layer wedding cake, with Deep portions of both imaging and spectroscopy, flanked by larger medium-depth regions. Bringing imaging and spectroscopy to bear on the same targets, while making efficient use of coordinated parallel observations, are driving goals of the survey design. Here we begin to describe these considerations.

The differing on-sky geometries of the NIRCam and NIRSpec instruments mean that these two cannot be efficiently overlapped with a single pointing of NIRCam. It takes at least a 2 x 2 mosaic of NIRCam to produce a filled area large enough to cover one NIRSpec MOS pointing. Further, the ability to use two instruments at once is an important opportunity to increase the science return, but the angular separation between the instantaneous fields of the instruments drives one to a large field. We note that, as a consequence of the visibility constraints, neither of the JADES fields allows JWST to return at a 180° position angle (P.A.), so as to swap the instrument locations. Instead, we have to construct an adequately sized mosaic, and choose the parallels to maximize the science return. Most of the MIRI parallel data and the NIRSpec MOS parallel data falls on NIRCam imaging, and nearly all of the NIRSpec parallel data falls on the GOODS/CANDELS HST imaging.

We placed the Deep portion of JADES in GOODS-S, while the Medium data are in both fields. We considered placing Deep pointings in GOODS-N, but as full support of the NIRSpec MOS footprint requires four NIRCam pointings, this would have become overly expensive.

The NIRCam data in JADES fall into four categories. There are contiguous portions in regular mosaics, of both deep and medium variety; we call these "Prime." Other portions occur as parallel exposures to NIRSpec MOS pointings, whose positions are therefore dictated by the location and position angle of the spectroscopy; we call these "Parallel." Again, these come in deep and medium variety.

In detail, 10 of the Medium-depth Prime NIRCam exposures were taken with NIRSpec in parallel, but the structure of JWST coordinated parallel observations is that NIRSpec is formally prime in the planning tool. We refer to NIRCam as prime (and NIRSpec as parallel) despite this, because the exact pointing and exposure times were being dictated by the NIRCam science goals.

Other NIRCam pointings were taken with MIRI in parallel; these yield Deep and Medium MIRI imaging.

The JADES NIRSpec MOS data fall into three tiers. One tier comprises two deep pointings, one scheduled early in the program and targeted without JWST imaging, the other scheduled at the end and targeted from the JADES imaging. These are called Deep/HST and Deep/JWST, respectively. Then, there are two tiers of medium depth, called Medium/HST and Medium/JWST for the same reason. Unlike the Deep pointings, Medium/HST is somewhat shallower than Medium/JWST. All of the NIRSpec MOS data is taken with NIRCam in parallel.

The Medium-depth designs with both NIRCam and NIRSpec MOS are shaped heavily by a desire to take well-dithered data, with at least 6 pixel locations to provide robustness to bad pixels and the undersampled point-spread function (PSF), and to use long enough exposures to keep observatory overheads low (these concerns are easily satisfied with the Deep data). Hence, even this flanking data is quite deep in comparison to pre-JWST opportunities. Because of the full use of coordinated parallel observations, we paid particular attention to minimizing the data rate for telemetry, typically utilizing the DEEP8 readout pattern for NIRCam and SLOW readouts for MIRI. This kept the program to about 2 GB hr^{-1} of data volume.

Although JADES was designed to be observed in a single year, over-scheduling in Cycle 1 resulted in it being scheduled over 18 months. In particular, the large investment in GOODS-S was spread over two observing seasons. This led to some reoptimization relative to the original design, induced by exact position angles, instrument problems for some observations, and further on-orbit appreciation of science opportunities. It also created a richer dataset for deep-sky infrared variability than originally planned (C. DeCoursey et al. 2025). We will focus in this paper on the observed program, making only passing mention of the original layout.

3.3. JADES Footprint

The footprint of the JADES survey is shown in Figure 3 for GOODS-S and Figure 4 for GOODS-N. As the geometry is complicated with the various overlapping footprints, we include separate images of each major portion of the survey.

In GOODS-S, one can see how the primary Deep portion of the survey, centered on the UDF, and the Medium portion to the west support each other with coordinated parallel observations. For instance, the MIRI parallels are largely partnered with NIRCam imaging, including the first NIRCam Deep Parallel. We also generate NIRSpec Medium/HST parallels that fall back on the UDF, providing high-multiplex spectroscopy for our Deep imaging. Finally, the NIRSpec Medium/JWST and Deep/JWST pointing create NIRCam parallels that fan out to create more imaging area.

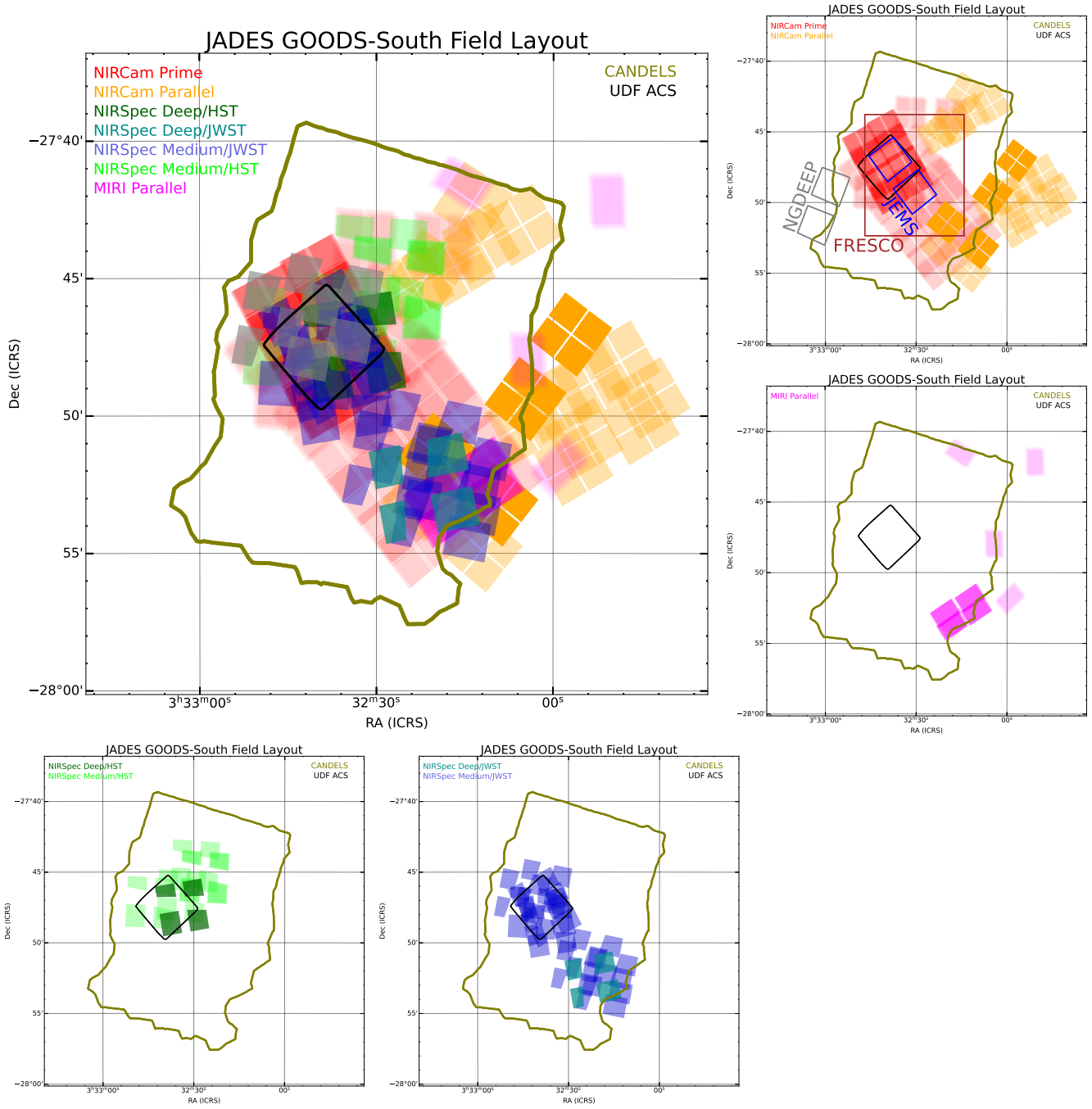

Figure 3. Layout of the JADES observations executed in the GOODS-South field. JADES observations with NIRCam, NIRSpec MOS, and MIRI are shown as colored shaded regions. Higher opacity indicates higher exposure time for NIRCam and MIRI or overlapping MSA pointings for NIRSpec. Dithers and nods smaller than 2″ are mostly not plotted. For NIRCam, only the SW quadrants are shown for clarity. For NIRSpec, only the active area of the MSA that was used for target placement, excluding regions that lead to truncated prism spectra, is shown. Two MIRI parallels with short F1500W exposures are not visualized. Outlines of other surveys, including the HST/ACS UDF and CANDELS, are shown with black and olive-green curves, respectively. The smaller subpanels show the same information split by instrument for clarity, because it can be difficult to see the details when all observations are plotted together. The NIRCam subplot in the upper-right panel additionally includes field outlines for the public JWST Cycle 1 NIRCam imaging from the JEMS, FRESCO, and NGDEEP programs.

In GOODS-N, the area of the prime survey is a little smaller, which makes it harder to fully utilize the parallels. We do utilize the NIRCam Medium Prime fields to cover the HDF and provide imaging for the initial NIRSpec Medium/HST spectroscopy as well as targets for the Medium/JWST follow-up. The parallels from that later spectroscopy produce NIRCam images that cover additional GOODS/CANDELS imaging. Two of the NIRCam prime pointings did not have MIRI or NIRSpec parallels that would fall on NIRCam imaging or GOODS; we opted to use MIRI, to be partnered with HST CANDELS imaging and perhaps future NIRCam data.

A major constraint on the layout of the survey comes from the intention to be able to conduct NIRSpec follow-up of NIRCam-selected targets within a single observing window. We judged that 60 days would be the minimum separation of these visits; this implies performing the NIRCam imaging early in the window and the NIRSpec follow-up late in the

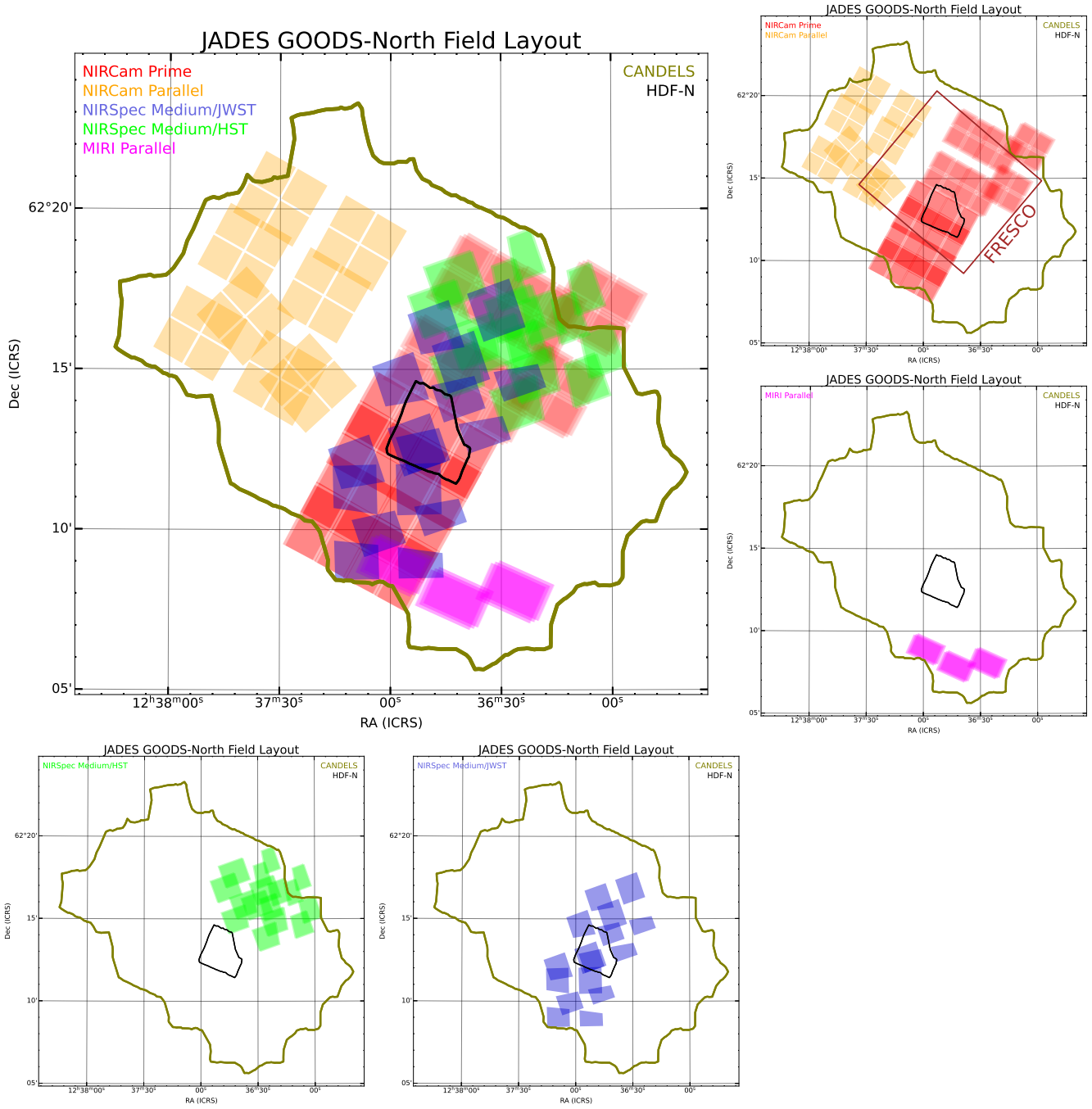

Figure 4. Layout of the JADES observations executed in the GOODS-North field. Details are the same as in Figure 3. The NIRCam subplot in the upper-right panel additionally includes the outlines of the public JWST Cycle 1 NIRCam imaging from the FRESCO program.

window. In GOODS-N, this plan was scheduled in this manner. In GOODS-S, because some of the imaging was delayed until year 2, we still chose to conduct the prime imaging early in the window and the spectroscopy late in the window.

In GOODS-S, the year 1 NIRCam Deep Prime imaging was taken at V3 P.A. = 298.°56, in early 2022 October. The year 1 Medium Prime imaging was taken a week later at V3 P.A. = 308°. The first NIRSpec Deep/HST pointing followed at V3 P.A. = 321°. In year 2, we sought to match the Deep Prime and Medium Prime position angles to those of year 1. This was successful for Deep, but observatory interruptions disturbed the Medium plans. The locations of the spectroscopic fields were chosen based on the exact availability of high-priority high-redshift candidates given the complex MSA constraints.

In GOODS-N, we observed the NIRCam Medium Prime data at P.A. = 241° in early 2023 February. The NIRSpec Medium/JWST data then followed in early May, at P.A. = 150.°48. Due to a fault with acquiring guide stars, one observation was skipped and had to be redesigned and observed at P.A. = 132.°93.

3.4. Other Overlapping JWST Data

The GOODS fields, UDF, and HDF have of course been observed by other programs in JWST Cycle 1 and Cycle 2.

Here we briefly describe programs whose data overlap JADES. Figures 3 and 4 show the JADES NIRCam footprint with overlays with some of these and other programs. We surely expect this list to grow in future cycles.

The First Reionization Epoch Spectroscopic Complete program (FRESCO; PI: Oesch, Program 1895; P. A. Oesch et al. 2023) conducted NIRCam F444W slitless spectroscopy (2 hr depth), paired with F182M and F210M medium-band imaging (1 hr each). These eight-pointing mosaics in GOODS-S and GOODS-N overlap heavily with JADES. FRESCO has proven to be highly complementary to JADES, as the strong emission lines are imaged as excesses in JADES photometry and then redshifts are obtained in FRESCO. The additional medium-band imaging, while shallower than JADES, provides more spectral resolution on mid-redshift galaxies.

The JWST Extragalactic Medium-band Survey (JEMS; PIs: Williams, Tacchella, & Maseda; Program 1963; C. C. Williams et al. 2023) observed one pointing on the UDF in F182M, F210M, F430M, F460M, and F480M, with 4–8 hr/filter. This dataset heavily overlaps with JADES, providing additional filters with compelling depth. In addition, JEMS conducted an NIRISS parallel in F430M and F480M, about half of which overlaps JADES NIRCam imaging.

Between these two, we note that F182M and F210M are available for a notable portion of JADES. We have coreduced JEMS and FRESCO NIRCam imaging with JADES, and include these data in JADES photometric catalogs.

In addition to FRESCO's wider medium-depth slitless spectroscopy, the Next Generation Deep Extragalactic Exploratory Public survey (NGDEEP, PI: Finkelstein, Program 2079) is producing very deep NIRISS slitless spectroscopy on the UDF (M. B. Bagley et al. 2023). We expect that these programs will complement the deeper but targeted NIRSpec MOS spectroscopy. The NGDEEP NIRCam imaging parallel falls off the JADES footprint, to the southeast.

There are also other deep MIRI GTO imaging programs in GOODS-S. The MIRI Deep Imaging Survey (Program 1283, PI: Oestlin; P. G. Pérez-González et al. 2024; G. Östlin et al. 2025) is observing one extremely deep pointing in the UDF, reaching 41 hr in F560W and 8.5 in F1000W. The NIRISS parallel from this pointing falls at the southern edge of JADES NIRCam imaging. For wider MIRI coverage, program 1207 (SMILES, PI: G. Rieke) is observing 15 pointings in eight filters, all overlapping the JADES NIRCam imaging (S. Alberts et al. 2024).

The push for deep imaging and spectroscopy in GOODS-S continued in Cycle 2 with an approved GO program 3215 (PI: Eisenstein) that returned to the footprint of the JADES 1210 program, now dubbed the JADES Origins Field, to add very deep NIRCam imaging in six medium bands—F162M, F182M, F210M, F250M, F300M, and F335M—to refine the search for $z > 15$ Lyman dropouts (D. J. Eisenstein et al. 2023). At the same time, ultradeep NIRSpec MOS spectroscopy was obtained on top of the JADES Deep Prime imaging.

The scheduling of JADES over 2 yr created new opportunities to study deep infrared time variability. This was pursued by a Director's Discretionary program 6541 (PI: Egami) to conduct NIRSpec MOS spectroscopy of transients and host galaxies in the Deep Prime region, as well as two additional epochs of multiband imaging.

Finally, there are several other NIRSpec programs in the fields. Two examples are program 2674 (PI: Arrabal Haro), which conducted NIRSpec MOS and coordinated NIRCam imaging in GOODS-N that complement the JADES footprint, and program 2198 (PI: Barrufet, L. Barrufet et al. 2025), which conducted NIRSpec MOS and NIRCam pre-imaging on two fields in GOODS-S. Other spectroscopic programs are the GTO NIRSpec WIDE MOS survey from programs 1211 and 1212 (PI: Luetzgendorf) and IFU program 1216 (PI: Luetzgendorf). Additional NIRCam pure-parallel imaging overlapping both fields is being obtained by the PANORAMIC program (PI: Williams, Program 2514, C. C. Williams et al. 2025) and program 3990 (PI: Morishita, T. Morishita et al. 2025).

4. NIRCam Observations

In this section, we detail the JADES NIRCam imaging. We begin by describing the details of the four categories of NIRCam imaging: Deep Prime, Medium Prime, Deep Parallel, and Medium Parallel. We then discuss cross-cutting aspects: filter selection, data quality, and a summary of depths.

4.1. NIRCam Deep Prime

In the heart of GOODS-S centered on the UDF, we observe four NIRCam fields to image a $4.'4$ by $6.'1$ rectangular field. A pair of NIRCam pointings is offset by $\sim 61.''5$ in V2 so as to cover the NIRCam intermodule gap, and each pointing contains many exposures including offsets in V3 to cover the short-wave chip gap. This pattern is then repeated in the second pair of pointings, offset in V3, leaving only a small overlap with the first pair. We size this offset to the height of the long-wave (LW) footprint, as this is slightly smaller than the short-wave (SW) footprint. We note that the mosaic was laid out for V3 P.A. of 300° but observed at $298.^\circ56$, causing a small cosmetic deviation from a rectangular layout.

We use the DEEP8 readout pattern with seven groups, yielding individual exposure times of 1375 s. DEEP8 was used to reduce the data volume, but does yield somewhat worse recovery from cosmic rays than a MEDIUM choice would have. In total, each pointing utilizes 114 such exposures, each with an SW and LW filter choice. Because each pointing includes more than 2 days of exposure time, we must split the observations into three visits. The first two use nine-point subpixel dithers (and no primary dither), each with five filter pairs, yielding 45 exposures. These two visits are offset in V3 by $\sim 5''$ to step over the SW chip gap. The third visit uses a mosaic of two pointings, each with 4 point subpixel dithers and three filter pairs, so 24 total exposures. The mosaic is designed with a row overlap chosen to result in the same V3 step and with the pointing chosen to result in the same footprint as the first two visits. Due to a mistake in correcting for a small P.A. shift, the third visit of pointing 2 is offset mildly, $3''$, from the exact overlap. All filters are included in both 9 point subpixel dither visits and therefore most points in the image are observed by at least 18 different NIRCam pixels (nine if the location falls in the SW chip gap in one of the visits).

These observations are all taken with MIRI in coordinated parallel, the results of which will be described in Section 6. Because of this, in the first season, we selected the subpixel dither based on F770W step sizes. After inspecting these results, we concluded that a mildly larger step size would be better for background subtraction; we therefore changed to the F1500W dither pattern in year 2.

Table 1
Overview of the NIRCam Deep Imaging in GOODS-S in Different Filters, Listing the Number of Separate Exposures and the Total Exposure Time per Pointing, in Kiloseconds

	Deep Prime		Parallel 1210		Parallel 1287	
Filter	N_{exp}	t_{exp}	N_{exp}	t_{exp}	N_{exp}	t_{exp}
F090W	26	35.7	36	49.5	24	33.0
F115W	44	60.5	48	66.0	42	57.8
F150W	26	35.7	36	49.5	24	33.0
F162M	…	…	…	…	18	24.7
F182M	…	…	…	…	18	24.7
F200W	18	24.7	24	33.0	18	24.7
F277W	26	35.7	30	41.2	18	24.7
F300M	…	…	…	…	18	24.7
F335M	18	24.7	18	24.7	18	24.7
F356W	18	24.7	24	33.0	24	33.0
F410M	26	35.7	36	49.5	30	41.3
F444W	26	35.7	36	49.5	36	49.5
Total	114	156.7	144	198.0	144	198.0

Note. We note that some Deep prime pointings overlap, doubling the depth, and that many Deep pointings also overlap with Medium, further increasing the depth.

We utilize nine filters in the Deep Prime pointings: F090W, F115W, F150W, and F200W on the SW arm, and F277W, F335M, F356W, F410M, and F444W on the LW arm. The exposure times per filter are listed in Table 1. It is important to note that about over a third of the total field is covered by two of the pointings, doubling the total exposure times. Because of the importance of high-redshift dropouts, we slant the SW exposure times toward the F115W and F150W filters, while on the LW side, we favor the longer filters where the zodiacal background is reducing the sensitivity. A comparison of the imaging we obtained in the NIRCam Deep Prime with that from the HUDF HST imaging is shown in Figure 5.

Although JADES was designed to be observed in 1 yr, Cycle 1 scheduling constraints caused the program to be split. We opted to observe all four pointings in each year. In year 1, all pointings were observed with one of the nine-point dither visits, and two were observed with the four-point dithers. This was repeated in year 2, completing the observing. Unfortunately, this segmentation also caused a delay in the spectroscopic follow-up of the Deep imaging. However, it did create an opportunity to consider year-scale time variation in this nearly 25 arcmin^2 deep field.

In total, this part of the JADES program was an investment of 229 hr and resulted in 174 open-shutter hours of data, a utilization of 76%.

4.2. NIRCam Medium Prime

To provide shallower flanking coverage and increase the area available for NIRSpec MOS targeting, JADES includes 18 pointings in (mostly) regular mosaics yielding contiguous coverage to medium depth. Seven of these are in GOODS-N and 11 in GOODS-S. Because of the footprint, eight of the pointings have MIRI in parallel, while 10 have NIRSpec MOS in parallel. In most cases, the pointings are paired with a 62″ step in V2 so as to fill a long rectangle covering the intermodule gap, with some double coverage. In detail, the step is chosen to match the width of one SW chip, so that the pointings cover the V3-parallel chip gap of their partner.

Cycle 1 scheduling constraints caused half of the Medium Prime time in GOODS-S to be delayed until fall 2023. We opted to observe in 2022 the six pointings of the mosaic that did not overlap the NIRCam Deep Prime field, so that most of the prime area could be observed in fall 2022, including the footprint of the deep MIRI parallels. These pointings also provided NIRSpec MOS parallels on and around the UDF. The GOODS-S mosaic was designed for a V3 P.A. of 308°. The small P.A. difference from the Deep Prime mosaic was included to make the program easier to schedule.

For these six pointings, the filters are as in Deep Prime save for omission of F335M. Each of the eight filters received six exposures, falling on six different pixels. The filter pair of F115W and F444W received 1159 s exposures using DEEP8 and six groups. The other three filter pairings receive 945 s exposures; these use DEEP8 with five groups to reduce data volume. Unfortunately, one pointing failed due to shorts in the NIRSpec MSA; this one was repeated in fall 2023. Another pointing had half of the LW imaging impacted by the shorts; we opted to accept this one and adjust a future pointing to compensate.

After this start, and in view of the ongoing scheduling of the NIRCam parallel observations, we opted to make some minor adjustments. We had originally planned for 19 Medium pointings, but we decided to remove one pointing in GOODS-S and compress certain exposure times in GOODS-N in order to add F335M back into filter set for 11 of the 12 remaining pointings, pairing with a second exposure of F115W. We also had to adjust times to balance the program within its allocation, due to small on-orbit alterations in the parallel observation timing model. In GOODS-N, we accomplished this by decreasing the time in the three pointings with MIRI parallels; in one case, we were unable to include F335M. The detailed exposure times are presented in Table 2 for GOODS-S and Table 3 for GOODS-N. Most exposures use the DEEP8 readout mode, but the shorter ones use MEDIUM8.

Unfortunately, for the five second-year pointings in GOODS-S, the observatory had a series of guide-star problems and a safing event during the observing period. Only two of the five fields were observed. Rather than wait a full year to return to form a mosaic at a single position angle, we opted to replan the remaining time to fill in specific holes in coverage around the flanks of the Deep Prime region. As will be discussed in Section 6, this resulted in a less-favorable location of the MIRI parallels.

In particular, observation 24 and most of 20 were observed at the originally planned location. Fortunately, these were the two most important to connecting to the first-year mosaic and making a wider mosaic around the Deep Prime region. Observation 20 was interrupted by an observatory safing before the last filter pair, F200W and F277W. We replanned to cover these two filters at a position angle 90° rotated, using two pointings (220 and 222) to cover each of the two NIRCam modules from observation 20. The second module was placed inside Deep Prime to increase the time-domain coverage of that field.

The remaining three pointings were replanned at PAs later in the observing window to address flaws in the coverage. Observation 219 served to cover the module gap of observation 20 and a thin remaining wedge between Deep

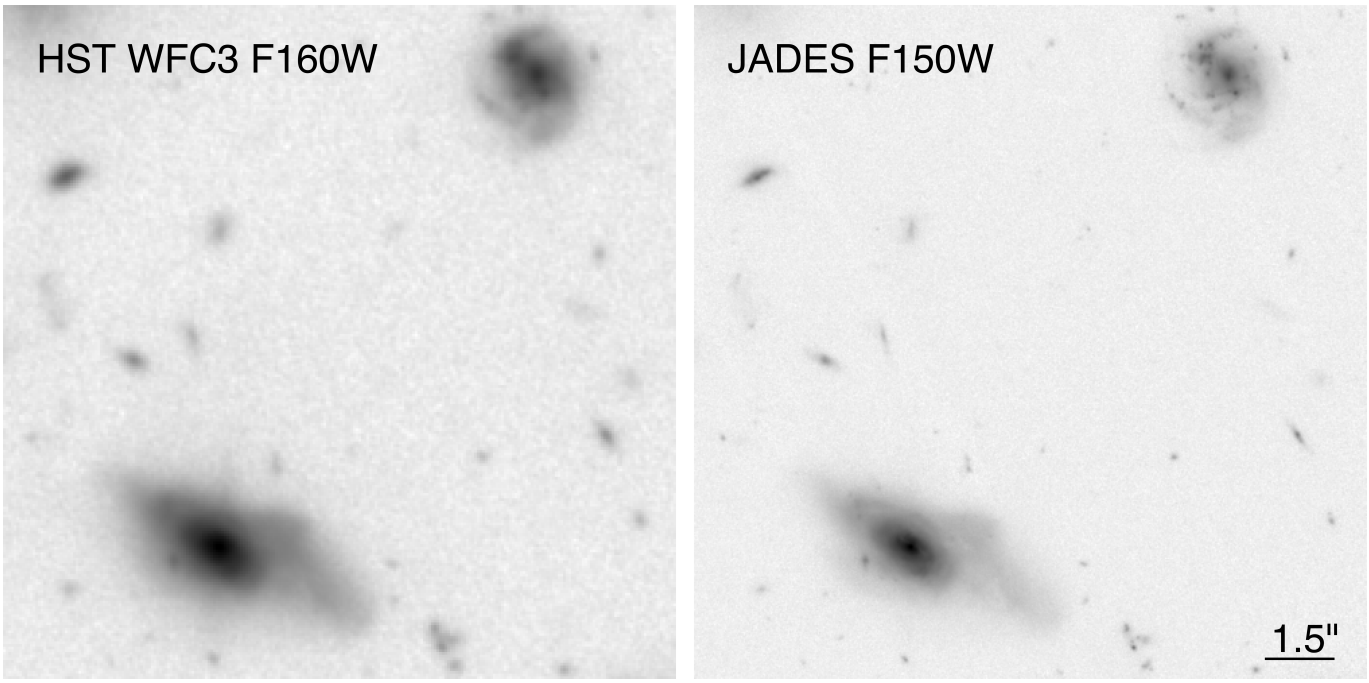

Figure 5. A small portion of the Hubble Ultra Deep Field, comparing HST and JWST imaging. Left panel: the F160W image from HST WFC3, from the Hubble Legacy Field reduction (G. Illingworth et al. 2016; K. E. Whitaker et al. 2019), with an exposure time of about 65 hr. This is the single deepest *H*-band image taken with HST. Right panel: the F150W JWST NIRCam image from the first year of JADES with an exposure time of about 10 hr . The superior depth and image quality of JWST is clear.

Table 2
Overview of the NIRCam GOODS-S Medium Imaging in Different Filters, Listing the Number of Separate Exposures and the Total Exposure Time per Pointing, in Kiloseconds

	with NS-HST		with MIRI		with MIRI Replan[a]		with NS-JWST	
Filter	N_{exp}	t_{exp}	N_{exp}	t_{exp}	N_{exp}	t_{exp}	N_{exp}	t_{exp}
F070W	…	…	…	…	…	…	6	5.03
F090W	6	5.67	6	6.96	6	5.67	9	8.50
F115W	6	6.96	12	11.34	12	11.34	12	10.05
F150W	6	5.67	6	6.96	6	5.67	9	8.50
F200W	6	5.67	6	5.67	6	5.03	9	7.54
F277W	6	5.67	6	5.67	6	5.03	9	8.50
F335M	…	…	6	5.67	6	5.67	6	5.03
F356W	6	5.67	6	5.67	6	5.67	9	7.54
F410M	6	5.67	6	6.96	6	5.67	9	8.50
F444W	6	6.96	6	6.96	6	5.67	12	10.05
Total	24	23.96	30	30.92	30	27.70	45	39.62

Notes. We note that some pointings overlap, increasing depth. Pointing 25 of Medium/HST set lost half of the LW exposure time to illumination from a short circuit in NIRSpec.
[a] Three pointings (observations 22, 219, and 223) with MIRI parallels were replanned and shortened to balance the time within the allocation. In addition, observation 20 missed its F200W and F277W filters, which were replaced with the shorter exposure time as observations 220 and 222.

Prime and the year-1 Medium mosaic. Observation 223 served to cover the module gap of observation 24 and increase time-domain coverage of the Deep Prime region. Observation 22 was placed to cover a remaining portion of the Medium/HST spectroscopy. All three of these are mildly shorter than observation 24 due to the need to balance the total time budget.

Table 3
Overview of the NIRCam GOODS-N Medium Imaging in Different Filters, Listing the Number of Separate Exposures and the Total Exposure Time per Pointing, in Kiloseconds

	with NS-HST		with MIRI P1&2		with MIRI P3		with NS-JWST	
Filter	N_{exp}	t_{exp}	N_{exp}	t_{exp}	N_{exp}	t_{exp}	N_{exp}	t_{exp}
F070W	…	…	…	…	…	…	6	5.67
F090W	6	5.67	6	3.09	6	3.09	12	11.34
F115W	12	11.34	12	6.18	6	3.74	12	11.34
F150W	6	5.67	6	3.09	6	3.09	9	8.50
F200W	6	5.67	6	3.09	6	3.09	6	5.67
F277W	6	5.67	6	3.09	6	3.09	9	8.50
F335M	6	5.67	6	3.09	…	…	6	5.67
F356W	6	5.67	6	3.09	6	3.09	6	5.67
F410M	6	5.67	6	3.09	6	3.74	12	11.34
F444W	6	5.67	6	3.09	6	3.09	12	11.34
Total	30	28.34	30	15.46	24	13.00	45	42.52

Note. We note that some pointings overlap, increasing depth. Pointing 3 (observation 3) with MIRI parallels is shorter than the other two to balance the time within the allocation. Pointings 4–7 are in concert with NIRSpec Medium/HST, while pointings 8–11 are with Medium/JWST.

For the seven pointings in GOODS-N, we pack four of them tightly in V2 to cover the intermodule gap. The other three have no intermodule coverage, and we further have chosen these to have less exposure time, as the MIRI parallels are more flexible than the NIRSpec MOS parallels. The northern portion of the mosaic is therefore somewhat shallower, but able to cover more of our early NIRSpec Medium/HST data. We decided that it was more important to maintain a sixfold dither than to insist on a filled footprint, expecting that this

field will likely attract larger coverage in future cycles. The mosaic was designed and observed at V3 P.A. of 241°.

Regarding the dither strategy, when operated with MIRI parallels, we use three dithers with the INTRAMODULEX pattern and two-point subdithers. These were based on the MIRI F1800W PSF in GOODS-N and F2100W in GOODS-S, chosen to increase the dither step size for background subtraction. This dither uses small steps at 45° in V2 and V3, stepping over both SW chip gaps in each. Hence, most points in the chip gaps receive four SW exposures; only small overlaps from the cross in the middle generate only two. We remind the reader that in most cases, the center of each arm is covered by the other pointing in the pair.

When operated with NIRSpec parallels, the strategy is mildly different. Here, we split the six exposures into two sets of three. Each triplet is a different MSA design with largely independent targets, to be described further in Section 5. In each triplet, NIRSpec executes its three-step nod along the slits of the MSA. We note that these steps are roughly at 45° on the NIRCam pixel grid. For the next triplet, we step the central pointing purely in the V3 direction by an amount to cover the V2-parallel chip gap. The V3-parallel gap is not covered within this pointing, but usually is by the partner in the mosaic.

In summary, this part of JADES was an investment of 195 hr, 123 in GOODS-S, and 72 in GOODS-N, resulting in 131 open-shutter hours (with the formally prime instrument), a utilization of 67%.

4.3. NIRCam Deep Parallel

In GOODS-S, JADES executes two long NIRSpec MOS pointings (Section 5), each of 200 ks open-shutter spectroscopy. Each of these is used to make a long NIRCam parallel exposure, the location of which depends on the position angle and observing window, which in turn was subject to the programmatic constraints of the NIRSpec targeting.

It turned out, fortuitously, that the first of these pointings, program 1210 (PI: Lützgendorf), was at a position angle (V3 P.A. of 321°) that caused the NIRCam parallel to fall on top of the deep MIRI parallels produced by the NIRCam Deep Prime program. This very deep region then became the optimal location for the deep medium-band imaging and deep spectroscopy of the Cycle 2 program 3215 (Program 3215; D. J. Eisenstein et al. 2023). This region has now been named the JADES Origins Field, with over a week of NIRCam observation on a single pointing.

The second pointing, program 1287 (PI: Lützgendorf), was required to be late in the observing window so that the targets resulting from the analysis of the full NIRCam dataset could be used. We were scheduled for a V3 P.A. of 53°, placing the NIRCam parallel northwest of the main mosaic. The exact location was set by the location of the most interesting high-redshift candidates for the prime spectroscopy.

The first deep parallel use the same nine filters as the Deep Prime program. For the second deep parallel, we added three additional medium-band filters, based on the success of this mode in program 3215; this will be discussed in Section 4.5. Each uses the same readout pattern as Deep Prime: seven groups yielding 1375 s integrations. Both use 144 such integrations for a total of 55 hr of open-shutter imaging, indeed mildly deeper than a single Deep Prime pointing (but without the overlaps of the mosaic). The exposure times per filter are shown in Table 1.

One limitation of these data is that NIRSpec only employs nine dither locations, three nod locations in each of three different MSA configurations. We were careful to arrange that each filter is observed at least twice at every location. In detail, the NIRSpec exposures are just over twice as long as the NIRCam integration, so each nod position results in a pair of back-to-back otherwise identical NIRCam integrations, 72 in all. We note that the dither pattern is set by the geometry of the NIRSpec MSA and therefore not tuned to the pixel scale of NIRCam; that said, the steps are not commensurate with the NIRCam pixel scale, and so the intrapixel behavior is sampled.

Another limitation is that the three MSA configurations in NIRSpec are stepped only a short distance $\sim 0\farcs8$, to limit the effects of distortions across the MSA and thereby increase the ability to keep high-priority targets well centered in shutters. This means that the dataset does not fill the SW chip gaps. On the flip side, the data maximize depth in the region that is covered. An example of the superb quality obtained in this program is shown in Figure 6.

4.4. NIRCam Medium Parallel

JADES executes 12 medium-depth NIRSpec MOS pointings, four in GOODS-N and eight in GOODS-S, to be described in Section 5. Each of these produces a NIRCam coordinated parallel observation, with a total of 45 exposures. The exposure times are given in Tables 2 and 3.

As these parallel fields were at risk to fall off of the HST GOODS and CANDELS imaging, depending on the final position angles, we opted to include the F070W filter in addition to the nine filters used in the Deep imaging. This improves isolation of $z \sim 5.5$ Lyα dropouts.

As with the NIRSpec Deep program, these observations also use nine closely spaced dither pointings, via three nod locations in each of three slit configurations. The SW chip gaps are not covered. We ensure that each NIRCam filter is observed in at least two of the three slits and, hence, at six dither locations. Two of the three slits have all 10 filters observed; the remaining one is missing F070W, F200W, F335M, and F356W. Therefore, the area covered by all 10 filters is reduced by a tiny amount.

As the prime spectroscopy is located on the NIRCam Prime mosaic, these Medium parallels in both GOODS-S and GOODS-N fall almost entirely outside of the NIRCam Prime footprint, thereby providing a substantial amount of additional area at medium depth. In GOODS-N, we observed at V3 P.A. of $150\fdg48$ and $132\fdg92$, placing the new imaging on the northeastern portion of the HST GOODS-N field. Because of the location of high-priority spectroscopic targets, these do not form a regular grid, but they are close enough to map a sizable near-contiguous region. By coincidence, the orientation of NIRCam in this parallel imaging is almost 90° rotated from the Prime imaging, leaving an obvious pattern for future observations to fill in the gap between the two. Unfortunately, a guide-star acquisition failure caused Observation 8 to be skipped, requiring a replan (Obs 98) that was observed a few weeks later with 18° of rotation relative to the other three pointings. We mention that although the NIRCam imaging in Observation 98 was successful, this observation suffered from problems in NIRSpec that resulted in its being reobserved as Observation 198 a year later. The pure-parallel opportunity for that visit was used by program 2514 (C. C. Williams et al. 2025) to add additional medium-band filters to this pointing.

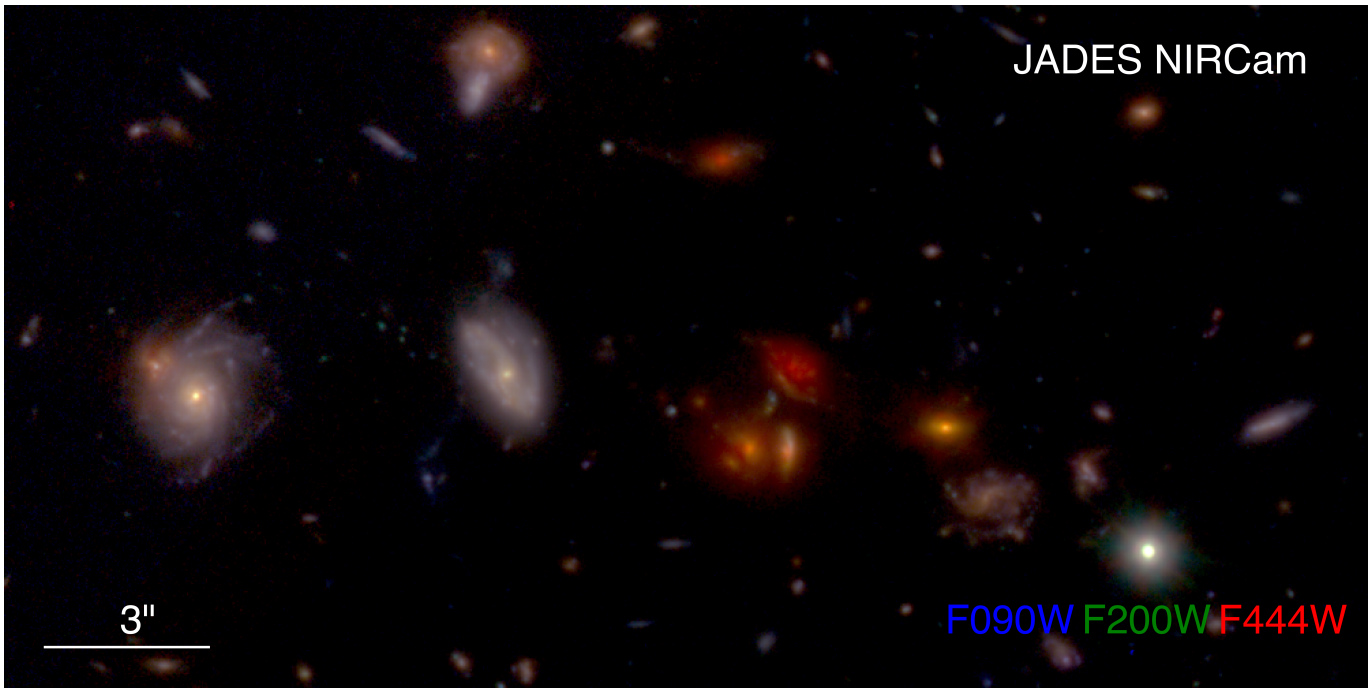

Figure 6. A small portion of JADES NIRCam GOODS-S imaging, combining F090W, F200W, and F444W filters in the Deep Parallel region of program 1210. This image shows the great diversity of galaxies revealed in every JWST image, with a wide variety of colors and morphologies. North is up.

In GOODS-S, we spread the spectroscopic pointings over the full Medium mosaic. In the original plan, these would all have been late in the first observing window, but given the scheduling delay, most were moved to the second year. The first field (observation 1) was observed on 2023 January 12–13, at a V3 P.A. of $56\overset{\circ}{.}17$. The second field (observation 5) was observed on 2023 October 19, at a V3 P.A. of $319\overset{\circ}{.}87$. The remaining six were observed 2023 December 12–19, at a V3 P. A. of $30\overset{\circ}{.}23$. We chose to use observation 5 on a NIRSpec region that placed the NIRCam parallel next to the JADES Origins Field in order to make this a wider footprint for future spectroscopy.

4.5. Comments on Filter Selection

Early on in the design of JADES, we recognized that the strong increase in zodiacal emission longward of 4.5 μm would increase the background in F444W, such that F410M could be competitive despite its narrower bandpass. We therefore opted to include both filters to increase the resolution of the SED. This is particularly important because of the strong rest-optical emission lines expected in some high-redshift galaxies, as indicated by Spitzer imaging and now confirmed with early JWST spectroscopy. The spacing of the Hα+[N II] and Hβ+[O III] complexes is such that only one can fall into F444W at any given redshift, and including F410M means that the comparison can separate the line from continuum emission at most redshifts (with ambiguity if the lines fall on the shoulder of the filter curves). This separation is important for stellar population modeling, as we want to measure the rest-optical continuum color relative to the ultraviolet.

As we studied this, we concluded that F335M and F356W offered a similar opportunity and that the likelihood of strong Hα or Hβ+[O III] emission recommended splitting this exposure time as well. This has been borne out in practice: we have found the ability to isolate strong emission lines at 3–5 μm to be very useful and interesting. In addition to the lines themselves, the extra spectral resolution helps to isolate the Balmer jump at high redshift and to measure the rest-optical continuum.

Where possible, we observe F277W somewhat longer than F356W because of the extra coverage from F335M. We keep F410M and F444W longer to compensate for the larger zodiacal background. Finally, we chose to slant the exposure time toward making F115W deeper, emphasizing the selection of $z > 9$ candidates.

In program 3215, we found that increasing the number of medium bands continued to provide very desirable access to emission lines and improved photometric redshifts. Therefore, we opted to echo much of this in our final deep parallel field, program 1287. By adding F300M, F182M, and F162M, we provide a single medium-band filter in each of F277W, F200W, and F150W. As before, this allows one to isolate a strong line from the continuum in each of these filters with a minimum of extra exposure time. We chose F182M and F300W as the most sensitive in each of these wide bands. We preferred F162M to F140M to keep consistent with program 3215 and because F162M and F182M provide improved Lyα dropout localization at redshifts above 12.

In summary, we have found the NIRCam coverage in the nine base bands to be highly effective for photometric redshifts. For example, at $z \approx 7$, one observes the Lyα drop in F090W and Hβ+[O III] in the longest bands. We further have found that the combination of medium and wide bands, particularly at the redder filters, is extremely helpful, as many of the higher-redshift galaxies have strong emission lines.

4.6. Data Quality Caveats

A detailed description of the data reduction and performance is presented elsewhere (M. J. Rieke et al. 2023b; F. D'Eugenio

et al. 2025). Here we describe some issues that we have already seen and that might be of interest to other users.

Our observing was split into many separate visits rather than long campaigns, and we encountered substantial persistence at the start of some visits, left over from the immediately preceding program. These signals last for several hours and will require detailed modeling and/or masking. The effect is more severe on the SW chips A3, B3, and B4; the other SW and both LW chips are much milder.

Most dramatically, in the Deep program, observations 7 and 10, were observed immediately after observations of the bright Trapezium nebula, leaving substantial diffuse emission over portions of SW chips A3, B3, and A4. This is most severe in the F090W filter (the first used), but there are faint traces in the next filter (F115W), 3.5 hr later.

We stress that the persistence is not simply coming from bright stars in the previous images, but the change in the diffuse background illumination level from the previous program. This greatly increases the affected area, particularly in A3 and B4. The decay time for A3 is particularly long. Observation 4 in 1181 shows a similar morphology of persistence incurred by a change in the background level relative to the previous program.

We also see persistence in A3 in visits following wave front sensing operations, creating a moderately sized ($\sim$100 pixel across) hexagonal image. While such sensing is common, the reference star is planned to fall on a consistent part of the chip. We suspect that the frequent reoccurence of this signal could allow that area of the chip to be particularly well characterized, but we have not attempted this. Note that 1180 observations 15 and 27, 1181 observation 9, 1286 observation 4, and 1287 visit 2 are affected by this. The chip used for wave front sensing has since been changed, avoiding this issue entirely.

We have also seen a case (1180 observation 18) in which a bright star happened to fall on the NIRCam field during the preceding MIRI observation, even though NIRCam was not being used in parallel. NIRCam is typically left open to the sky when not used. One can see the imprint of the whole MIRI dither pattern, as well as the trail when the telescope slewed away from the field.

Of course, these regions do also incur persistence from brighter sources in our own observations. For instance, in 1181 observation 2, there is a bright star in the bad portion of A3 that creates a recurrent glow in all six dither locations. And 1286 observation 8 contains the persistent glow of a bright star in observation 6.

Mitigating these persistent signals is particularly vexing when one is using a small-angle dither, as a pixel may never find a blank-sky location away from a larger galaxy. We therefore increased our subpixel dither selection in the later portion of our observations. However, this is not always possible when observing jointly with NIRSpec. We caution that we have not yet considered the effect of persistence on our photometry, but in the worst regions of these chips, we believe this should be studied. By construction, the dither pattern is repeated between filters, so the persistence from the first filter will affect the next.

Like many NIRCam observations, we occasionally have noticeable illumination of the SW detector through an off-axis stray-light path, producing the so-called "wisps." These affect F200W and F150W most strongly. While these signals are known to modulate in amplitude due to the brightness of stars in the source region on the sky, we have found that the exact morphology of the pattern also varies within our program. We are still analyzing this, but hope that a low-dimensional set of templates will suffice to remove them.

We have found it very helpful to visualize the calibrated exposures of a dither sequence in animations, fixed in pixel coordinates so that the true objects move and the detector artifacts stay still.

We have found it easier to disentangle persistence from wisps when F090W or F115W are observed first in a visit, so that the persistence has decayed away before the wisp-affected F150W and F200W bands are observed.

We now turn to rarer problems. The second half of one pointing (observation 30) of the Medium Prime mosaic in GOODS-S had to be skipped due to an onboard issue unrelated to our program. There was not enough time in the observing window (constrained by the spectroscopic coordinated parallel) to try again. Fortunately, this pointing is at the edge of the mosaic. The first half of this same pointing had its LW data badly contaminated by a glowing short circuit in the NIRSpec MSA. We repeated this entire pointing in 2023 October to complete the six-dither coverage; this means that the SW data in this pointing is 50% longer than normal.

One half of another pointing (observation 25, first four dither sequences) was also affected by the NIRSpec glowing short (T. D. Rawle et al. 2022). In this case, because the location of the field was favorable to access in a different way in the year 2 observing, we opted not to repeat this imaging location but instead combine the NIRSpec redo with another pointing.

In both of these cases, we found that the LW data were badly affected. The background was roughly doubled, but further, there are many patterns of concentric rings, with spacing depending on wavelength, likely due to some diffractive pattern from where the light from NIRSpec has bounced off of the tertiary mirror. As the short circuit is apparently not particularly hot, the effect on SW is much less, and we believe this data is usable. There are a handful of faintly detected rings in F200W, chips A1, A2, A4, and B4.

Next, in the three deep visits of 1210, we find an enigmatic set of arcsecond-scale blobs near an edge of B3. These are bright in the second visit, but detectable in the other two as well as in the 3215 imaging in year 2. They are therefore not due to persistence, and we are confident they are not astrophysical, as they do not appear in 1180 images of the same region. They also appear in other nearby pointings at this P.A. (observation 1 of program 5997) despite an arcminute change in pointing. The morphology is very different from a wisp, and importantly, they appear in both SW and LW images.

Some of the 1210 exposures have a plume of what appears to be scattered light in a corner of B4. We hypothesize that this may be due to a bright star striking the chip mask, as the signal changes slightly between the three visits of 1210, which move only at the arcsecond level, suggesting a well-focused source. However, we also see it in observations 27, 28, 29, and 30 of 1180, so it seems that the cause is not particularly rare.

Observation 219 of program 1180 suffers from a spray of light in A4 that we believe to be a bright star glinting off something just above the focal plane, as the amplitude is modulated by small dithers. There is also weaker stray light in A2 that we think is connected to this.

Table 4
Summary of Average Exposure Times and Depths in the NIRCam Deep and Medium Surveys

Filter	Deepest (9 arcmin^2)			Deep (33 arcmin^2)			Medium (167 arcmin^2)		
	Time (ks)	PS Depth (AB)		Time (ks)	PS Depth (AB)		Time (ks)	PS Depth (AB)	
		ETC	On-sky		ETC	On-sky		ETC	On-sky
F070W[a]	…	…	…	…	…	…	7.1	28.14	28.20
F090W	71.0	29.59	29.70	44.1	29.33	29.42	11.2	28.58	28.70
F115W	122.9	29.99	29.98	69.2	29.68	29.67	14.4	28.83	28.87
F150W	72.5	29.96	29.90	43.7	29.69	29.61	9.8	28.87	28.85
F162M[b]	…	…	…	24.7	28.87	28.90	…	…	…
F182M[b]	…	…	…	24.7	29.10	29.12	…	…	…
F200W	52.6	29.93	29.86	31.8	29.66	29.60	8.0	28.91	28.87
F277W	75.4	30.23	30.21	41.0	29.90	29.90	9.5	29.10	29.17
F300M[b]	…	…	…	24.7	29.13	29.10	…	…	…
F335M[c]	51.7	29.58	29.58	28.6	29.26	29.24	7.1	28.51	28.61
F356W	51.7	30.02	30.04	34.2	29.80	29.80	8.0	29.01	29.08
F410M	71.7	29.40	29.34	47.5	29.18	29.17	11.1	28.39	28.50
F444W	73.7	29.61	29.69	49.7	29.40	29.44	11.7	28.61	28.72

Notes. The six Deep pointings cover a total footprint of ∼42 arcmin^2, with around nine of these being double-covered and marked as Deepest. The 30 Medium pointings cover a total additional footprint of ∼167 arcmin^2 exclusive of the Deep footprint. Within each, we compute the average exposure time per filter, including the contribution of Medium to the deeper regions. We then present the 10σ 0.″2 diameter aperture depth, including point-source aperture correction, for these average exposure times, based on the JWST Exposure Time Calculator and separately from the variance of random apertures measured on the mosaics.
[a] The F070W filter is used in only a subset of Medium pointings, covering an area of ∼82 arcmin^2.
[b] The F162M, F182M, and F300M filters are used only in the single 1287 Deep pointing, covering an area of ∼9 arcmin^2.
[c] The F335M filter is not used in some Medium pointings, so that this filter covers a Medium footprint of ∼140 arcmin^2. In all three cases, we quote the average exposure time and depth in the smaller region.

Observation 98 of program 1181 displays stray light on multiple chips, probably from a bright star on the B4 chip. This stray light appears in both modules and both SW and LW, and it is not morphologically connected to the bright star. Clearly there is some complicated reflection path. Fortunately, much of the image area is usable. We see a weaker version of this in observation 11 of program 1181.

4.7. NIRCam Imaging Depth

As shown in Figures 3 and 4, the NIRCam pointings often overlap, so that the survey is deeper than what appears in Tables 1–3. Further, the depth varies because of the geometry of these overlaps. To provide a useful summary of the NIRCam program, in Table 4 we divide the footprint into three disjoint regions: Deepest, Deep, and Medium. Deepest refers to the area where two or more of the Deep Prime pointings overlap. Deep refers to the remainder of the area of the Deep Prime and Parallel fields. Medium refers to the rest of the area, including both GOODS-S and GOODS-N. In each case, the quoted areas are based on exposure time maps where we have required both F090W and F356W data and have required at least 2400 s in each filter to remove the outermost trim with only two to three dithered exposures. Only exposures from the Cycle 1 JADES program (PIDs 1180, 1181, 1210, 1286, 1287) are included. Masked pixels are included in the area estimate. We then compute the mean exposure time in each filter in each footprint. As this method uses the total exposure time maps, Medium pointings overlapping Deep regions are included in the Deep tally. We remind the reader that the exposure times do vary within the regions; for example, the northern portion of GOODS-N is shallower by a factor of 2–3 in exposure time than the bulk of the Medium region, while in some places, multiple Medium Parallel pointings overlap to approach Deep depth. Nevertheless, these summaries are reasonable averages for forecasts and contextual comparisons.

We then convert the representative exposure times to anticipated 10σ depths for background-limited 0.″2 diameter apertures with point-source aperture corrections. We do this in two ways. The first is to use the JWST Exposure Time Calculator. Here we assume the integration length of the Deep Prime program and observations in October. Spotchecking for other observations in JADES suggests that variations from this would be at the few percent level in depth. The second method is to measure the variance in many apertures in blank regions of the mosaic that have similar exposure time to the mean of the tier, scaling those apertures by the square root of the ratio of each exposure time to the reference value. We find that these two estimates are very similar, which is both a successful validation of the JWST Exposure Time Calculator and a finding that JADES is achieving the hoped-for scaling of depth with exposure time, i.e., there is not a floor from systematic imaging errors.

We remind the reader that the Deep area is all in GOODS-S, while the medium area is split approximately evenly between GOODS-S and GOODS-N. The average depths in GOODS-N are mildly shallower than in GOODS-S, but the two fields are sufficiently similar that we do not separate them for this summary.

In Figure 7, we show a visualization of the estimated depth of the JADES, JEMS, and FRESCO NIRCam and JADES MIRI imaging, along with the estimates for HST ACS and WFC3 imaging (K. E. Whitaker et al. 2019) in the HUDF and CANDELS fields that JADES overlaps. We have measured the JEMS and FRESCO depths in the same manner as that of JADES, using our own reductions of these data. One sees that the JADES imaging is comparable in depth in the deepest HUDF data, which covered only a single HST pointing. One

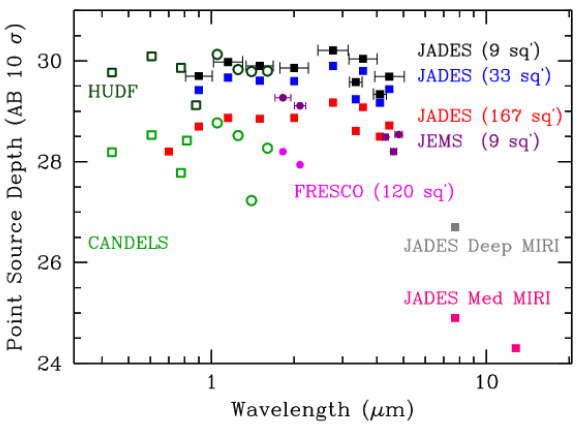

Figure 7. Depth vs. wavelength for JADES and other datasets. Black, blue, and red solid squares show the 10σ point-source depth for JADES Deepest, Deep, and Medium NIRCam data, using the variation in $0\farcs2$ blank-sky apertures. Purple and magenta circles show the depth of the JEMS and FRESCO medium-band imaging. Horizontal ranges show the filter widths. The JADES Deep and Medium MIRI depths are shown with gray and pink points on the right. The $0\farcs2$ aperture is mildly too small for the HST WFC3 image quality, causing these estimates of depth to be too optimistic by 0.1–0.2 mag compared to larger apertures. Comparison is shown (dark and light green) to the depths measured in the same method from the Hubble Legacy Field (K. E. Whitaker et al. 2019) mosaics, separating the single HUDF pointing from the broader CANDELS region. The HUDF ACS (WFC3) footprint is 11 (4.7) square arcminutes, comparable to the area of the Deepest JADES data. The CANDELS area exceeds the JADES Medium area. JADES improves over even the HUDF in area and spatial resolution, and at wavelengths longward of 1.6 μm, the gains in depth and resolution are immense.

also sees that the ratio of optical ACS to infrared JADES depth is less favorable in the broader CANDELS region compared to that of the HUDF.

5. NIRSpec Observations

As introduced in Section 3, the JADES NIRSpec MOS data fall into three tiers: Deep, Medium/JWST, and Medium/HST. All three tiers use the low-resolution prism as well as several gratings, with grating spectra available for most of the prism targets. Table 5 provides a summary of disperser configurations and exposure times for each tier. This section presents some of the features common to all tiers before describing each tier in turn.

Each of the NIRSpec gratings are used with a matching long-pass filter to prevent overlap of first order spectra by higher orders. For the band 1 G140M grating, there are two available filters: F070LP and F100LP. F100LP blocks all light below 1 μm, thereby ensuring no second-order overlap within the nominal spectral range up to 1.8 μm. F070LP allows through light at >0.7 μm, so it has the advantage of enabling observation in the range 0.7–1.0 μm. This corresponds to the wavelength of the Lyα transition at redshifts of 4.8–7.2, bridging the epoch of the end of cosmic reionization (B. E. Robertson 2022). Therefore, we chose to use the F070LP filter for all of the JADES G140M spectroscopy. We accept that there will be second-order overlap from the sky, increasing the sky background at >1.4 μm, and from galaxies at redshifts below 7 that have flux in this wavelength region. However, much like the overlapping grating spectra allowed by our MSA configurations described in the following subsection, this increased continuum flux has little impact on our emission-line measurements from the G140M spectra.

5.1. MSA Configuration Design

JADES designed its NIRSpec multiobject observations using the tool eMPT (N. Bonaventura et al. 2023) that provided key features beyond what was found in the baseline tools for MSA design. In particular, eMPT allowed us to:

1. Constrain the NIRSpec pointings to a rigid mosaic of NIRCam fields, once the position angle is specified.
2. Impose a detailed prioritization system for our targets and have complete control over the order in which each class of targets is attempted to be placed on the MSA at a given pointing.
3. Optimize repeated observations across multiple overlapping MSA designs to maximize exposure time on the highest-priority targets.
4. Identify and eliminate beforehand targets having contaminating objects falling within their (nodded) slitlets.
5. Avoid the use of shutters leading to prism spectra truncated by the NIRSpec detector gap or contaminated by the spectra of failed open shutters.
6. Enable overlap of the grating spectra (except for some high-priority targets whose grating spectra are protected from overlap) to maximize the gratings multiplexing, while keeping those of the prism distinct.
7. Open additional blank-sky shutters that disperse onto unused detector real estate to support master background subtraction.

To do this, eMPT contains the full NIRSpec model of the astrometric distortions and multishutter geometry and constraints, from which it can accurately predict how given astrometric positions will fall onto shutters, whether those shutters are available to use, and where the resulting spectra will fall on the detectors (and thereby whether they will overlap). The code thereby revealed the detailed outcome of each target, with which one can proceed to accept targets in complex priority orders. After this process determines which shutters were to be opened, the final optimal pointings and matching MSA masks were imported into the standard APT/MPT workflow for further execution.

The MSA shutters are on a rigid grid, and the opaque regions between the shutters block enough light from compact sources that one typically chooses to retain only the fraction of targets that are sufficiently well centered in their shutters. Not all shutters function properly, with 22 failed open that always disperse light onto the detector and 17.5% of the unvignetted shutters that are permanently closed (T. Böker et al. 2023). Our MSA masks require a three-shutter-high slitlet for nodding and background subtraction. Locations where one can open a three-shutter-high slitlet are therefore limited by this MSA operability, leading to the concept of a "viable slitlet" map. In all of the JADES tiers, we perform MSA reconfigurations with small (always <10 and mostly $<1''$) offsets where we attempt to obtain spectra of at least the highest-priority targets in multiple configurations. Simulations have shown that these offsets need to be kept small to maximize the overlap of the viable slitlet maps and to avoid the astrometric distortion at the NIRSpec MSA plane that causes some objects to become insufficiently centered. For most tiers of JADES, the main constraint on these offsets is to ensure maximal coverage of the highest-priority targets in multiple MSA configurations.

Because of these constraints, one needs a very high target density in order to achieve a high multiplex of assigned targets.

Table 5
Summary of the NIRSpec MOS Observations

Subsurvey	Program	No. Fields	Subpointings	No. Targets	Exposure Times (ks)				
					Prism	G140M	G235M	G395M	G395H
GOODS-S Deep/HST	1210	1	3	253	100	25	25	25	25
GOODS-S Deep/JWST	1287	1	3	235	100	25	25	25	25
GOODS-S Medium/HST	1180	5[a]	1	677	3.8	3.1	3.1	3.1	⋯
GOODS-S Redo Obs 134	1180	1[c]	2	185	7.5	6.2	6.2	6.2	⋯
GOODS-S Redo Obs 135	1180	1[c]	3	185	11.3	9.3	9.3	9.3	⋯
GOODS-S Redo Obs 136	1180	1[c]	2	169	7.5	6.2	6.2	6.2	⋯
GOODS-S Medium/JWST	1286	8	3	1490	8.0	8.0	9.3	9.3	8.0
GOODS-N Medium/HST	1181	8[a]	1	853	6.2	3.1	3.1	3.1	⋯
GOODS-N Medium/JWST	1181	4	3	950	9.3	9.3	9.3	9.3	9.3

Notes. For each program, we list the number of separate MSA fields, as well as the exposure time per disperser in kiloseconds. Each field consists of one to three subpointings, each with two nearly identical MSA designs: one for the prism and a second for the grating; the latter closes a few shutters to protect certain high-priority spectra from overlap. The quoted times are summed over the subpointings, but not all targets can be placed on all subpointings. The number of unique targets in each subsurvey is listed; a small number of targets are repeated between rows. The long-pass filter choices for the gratings are F070LP, F170LP, F290LP, and F290LP, respectively.

[a] Each Medium/HST pointing is split into two distinct MSA locations, separated by the primary dither step across the NIRCam SW chip gaps. As the larger dither causes us to typically observe distinct galaxies, we count each pointing as two fields with one subpointing. When the slit registrations are favorable, we do reobserve high-priority targets to double the exposure times on these.

[b] Twelve MSA locations were planned, but only five were completed due to instrument problems.

[c] These seven redos were organized to be similar to three Medium/JWST locations, one with three subpositions and two with two subpositions.

JADES typically supplies at least 200 targets per square arcminute, yielding about 150 assigned targets on the prism designs, corresponding to an average assignment rate of only 9%. An obvious consequence of this low average rate is that one does not want to serve the rarer higher-value targets in this limited way. We therefore developed a detailed prioritization of the targets, largely by redshift and flux (see Section 5.2). The eMPT allows us to assign slits in a greedy order, assigning higher priorities first. While this slightly decreases the total multiplex, it yields much higher assignment rates on high value targets.

NIRSpec prism spectra have relatively short traces, allowing for multiple columns of nonoverlapping spectra. For a given prism MSA design, there is a matching grating MSA design that is nearly identical. Importantly, we keep nearly all of the same shutters open for the grating configuration so that most of our galaxies have information at multiple spectral resolutions. The longer traces of the gratings may overlap, as may the zero-order emission, but the emission lines are sparse in these spectra. Emission lines can be associated to their parent object in multiple ways: the location along the three-shutter-tall 1.″5 slit, the prism spectrum, where the lines appear unoverlapped, and the wavelength ratio of multiple detections. The dispersed continua of the typical faint targets are below the detector noise in the grating spectra, and hence, the continua of the overlapping spectra do not substantially increase the noise. For the highest-priority targets and for the infrequent brighter targets, we do close some shutters to avoid overlap; so, a small fraction of objects is observed only with the prism.

5.2. Target Prioritization

Here we summarize the design of the JADES spectroscopic target selection process. The main criteria for placing galaxies into priority classes are their redshifts and fluxes. Redshifts are estimated via photometric redshift algorithms and/or Lyman-break color selection. The highest redshifts are prioritized both because they are rare and because one of the main scientific goals of JADES is to understand the earliest phase of galaxy evolution. Galaxies with higher fluxes (in continuum or predicted emission lines, depending on the category) are prioritized since higher-S/N spectra allow for a wider range of science investigations.

The details of the priority classes depend on the tier (Deep, Medium/JWST, or Medium/HST) and whether the targeting is based only on HST imaging or on the JADES imaging. Deeper spectroscopic observations have lower flux limits for similar classes, so that the achieved S/N will be similar for the different tiers.

The highest-priority class contains relatively bright galaxies at the highest redshifts; $z > 8.5$ for Deep and Medium/JWST and $z > 5.7$ for Medium/HST program. After these, we prioritize fainter galaxies at the same redshift and then progressively lower-redshift bins, favoring the brighter galaxies. Through this, we aim to build up a statistical sample between redshift $1.5 < z < 5.7$ in the lower-priority classes over the tiers, with the shallower tiers contributing to the bright end, and deeper tiers contributing to the faint end. In addition to these classes, we also include a small fraction of galaxies identified as special in other data, e.g., with ALMA, Chandra, Lyα emitters selected with the ESO Very Large Telescope/MUSE instrument.

We also prioritize a few bright ($H_{AB} < 23.5$) moderate-redshift ($z > 1.5$) galaxies, enabling the collection of exquisite infrared spectra from objects around cosmic noon. After these, we prioritize in photometric redshift bins, favoring the rarer brighter examples. Galaxies with photometric redshifts below 1.5 are used as a low-priority filler sample; nevertheless, the large number of these targets yields a substantial observed set. Further details on the target prioritization, including variations

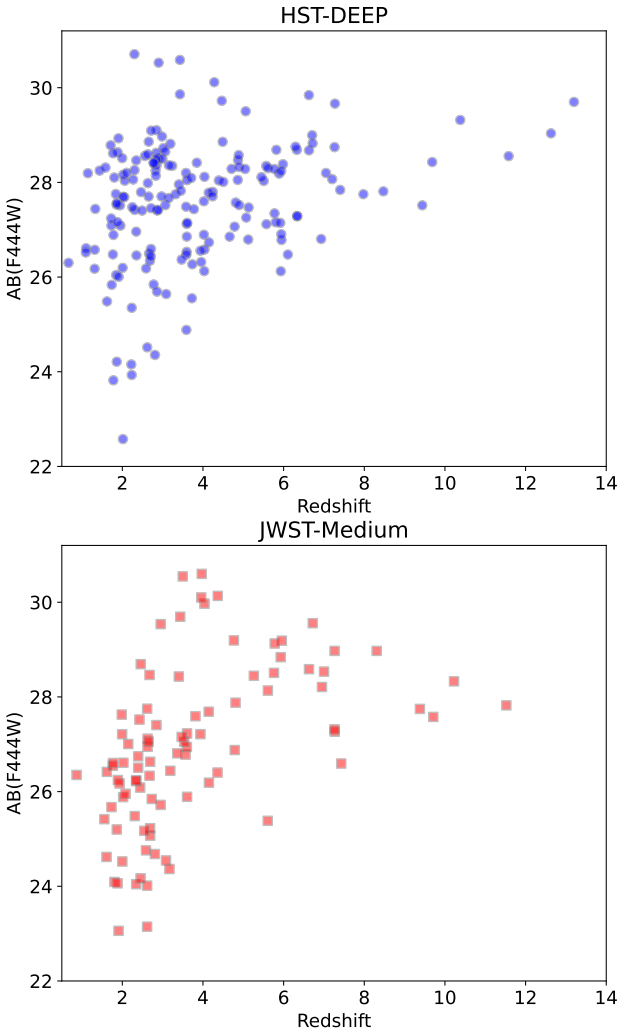

Figure 8. The observed distribution of F444W AB magnitude vs. spectroscopic redshift for the Deep/HST pointing (upper panel) and the first Medium/JWST pointing (lower panel). The target selection has successfully weighted toward higher-redshift galaxies, resulting in a more even redshift distribution.

per tier, are provided in the JADES data release papers (A. J. Bunker et al. 2024; F. D'Eugenio et al. 2025).

The distribution of spectroscopic redshift and F444W magnitudes are shown in Figure 8. One sees that NIRSpec is recovering redshifts to extremely faint flux levels, particularly in the Deep pointing.

5.3. MSA Target Acquisition

Successful use of NIRSpec MOS depends critically on high-quality astrometry. Astrometric distortions in the target coordinates tend to perturb targets away from the centers of their shutters, lowering performance. More insidiously, NIRSpec MSA Target Acquisition relies on a few bright compact sources to align the MSA to the desired location on the sky, so astrometric errors on those few objects can cause the entire MSA to be misaligned.

JADES was fortunate to be able to utilize recent reductions of HST imaging in the GOODS fields that had been aligned to the Gaia DR2 reference frame (G. Brammer 2025, private communication; Gaia Collaboration et al. 2016, 2018). This alleviated concerns of distortions or mismatches between faint targets and bright acquisition sources.

However, the GOODS-S and GOODS-N fields, being intentionally placed in regions of very low stellar density, do present a severe deficit of stars suitable for target acquisition. Instead, we had to use the HST imaging to identify compact galaxies, using the longest exposure time for the acquisition image to reach down to 24–27 mag. All of the JADES target acquisitions so far were successful, although the increased centroiding error for such extended targets may somewhat have reduced the alignment accuracy of the NIRSpec observations. In later spectroscopy, when NIRCam data was available, we used its imaging to select roughly circular compact galaxies and stars, using the multiband near-IR photometry to more confidently estimate the fluxes in the NIRSpec CLEAR and F140X target acquisition filters and to enforce isolation criteria. All candidates were visually inspected to reject a portion of objects that were lopsided, flattened, or insufficiently isolated; we aimed to be conservative in providing compact sources.

5.4. NIRSpec Deep Spectroscopy

JADES features two long NIRSpec multiobject observations, each of 200 ks total exposure time and both located in GOODS-S on the UDF and mostly inside the NIRCam Deep Prime footprint. The first pointing was designed to be observed early and be targeted using HST GOODS and CANDELS imaging, supplemented with other pre-JADES data. The second deep pointing was observed at the end of the program, using targets from the full JADES imaging. We refer to these two pointings as Deep/HST and Deep/JWST, respectively.

The NIRSpec Deep/HST observations occurred over three visits between 2022 October 21 and 25 at a V3PA of 321°. As described above, these observations were intended to be targeted solely on pre-JWST data. Shortly before the scheduled visits, NIRSpec suffered some shorts on the MSA that required us to replan the MSA configurations for these observations. The NIRCam Deep Prime data were taken at the start of October, and an early reduction of the multiband images and photometry catalogs were available. This enabled us to include some JWST-selected targets, at the expense of lower-priority HST-selected targets, in the NIRSpec observations. We also reprioritized the catalog using the NIRCam data to improve high-redshift photometric redshift accuracy, and to homogenize the selection in the lower-priority classes with respect to the Deep/JWST to be based on the F444W filter. We note that the pointings of the observations were not changed, only the choice of which shutters to open. Two of the additional target galaxies with photometric redshifts from the NIRCam imaging (B. E. Robertson et al. 2023a) were spectroscopically confirmed in Deep/HST to lie at the highest redshifts known of 12.6 and 13.2 (E. Curtis-Lake et al. 2023).

The NIRSpec Deep/JWST observations occurred over three visits on 2024 January 10–12, at a V3 P.A. of 53°. While we had originally expected for this pointing to be in the Deep Prime region, we found that the most attractive high-redshift candidates in JADES imaging were in and around the JADES Origins Field, with the very deep program 1210 and 3215 imaging. We therefore shifted the pointing. Unfortunately, the second of the three visits was skipped due to a telescope guide-star acquisition failure; this visit was observed a year later in 2025 January 12–13, with no changes from the original design.

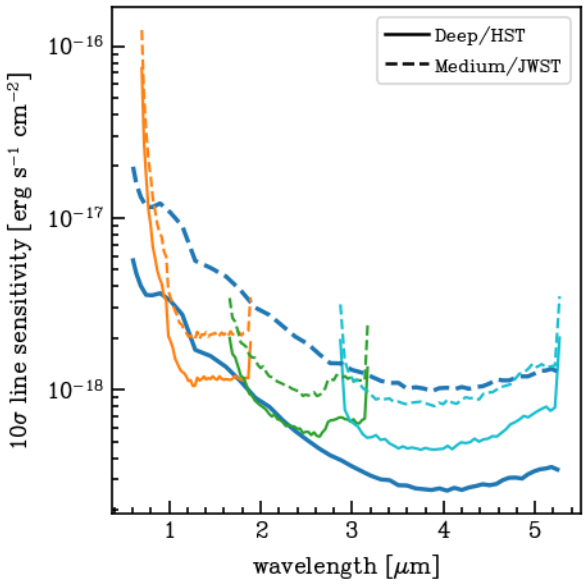

Figure 9. The unresolved line detection limit as a function of wavelength for two JADES NIRSpec tiers. We assume a well-centered point source and use a 10σ detection threshold. The blue long lines are the prism, while the orange, green, and cyan lines are the three $R = 1000$ gratings. The solid lines show the depth in the Deep/HST pointing, while the dashed lines are a representative Medium/JWST pointing. For an unresolved line, the G395H grating has a similar line detection limit to G395M plotted here.

The NIRSpec Deep spectroscopy utilizes five dispersers: the prism and four gratings: G140M/F070LP, G235M/F170LP, G395M/F290LP, and G395H/F290LP. The prism is observed for 100 ks, and the gratings for 25 ks each.

Each pointing uses slitlets of three shutters, with the three-point nod. To provide additional pixel diversity and some dithering in the spectral direction, we design three subpointings for each pointing, typically separated by three to five shutters in the dispersion direction and one to two shutters in the spatial direction such that the optimal common coverage of the highest-priority targets in all three dithered pointings is achieved. This results in the target light from a given wavelength for the majority of sources appearing in up to 9 pixel locations. As described earlier, there are actually two MSA designs for each subpointing (six in total) because we use a separate configuration for the prism relative to that of the gratings. Each integration uses NRSIRS2 readout with 19 groups, yielding 1400 s apiece. We conduct two integrations per exposure. For the gratings, this means that each nod location is visited only once for two consecutive integrations. For the prism, the telescope repeats the nodding four times, with two integrations per time.

As discussed in Section 5.1, it is inevitable that not all targets can be placed on all three subpointings, even though this is our preference for high-priority targets. We accept this and fill in some targets with only one or two subpointings. Using a smaller dither step increases the ability to repeat targets. For lower-priority targets, we prefer to change targets between subpointings, so as to maximize the number of distinct objects, as described in A. J. Bunker et al. (2024).

This part of JADES is an investment of 145 hr and results in 111 prime open-shutter hours, a utilization of 76%. The exceptional line-flux sensitivity achieved as a function of wavelength is shown in Figure 9.

5.5. NIRSpec Medium/JWST Spectroscopy

JADES includes 12 medium-depth pointings that are targeted from JWST imaging but otherwise scaled down versions of the Deep pointings. Relative to Deep, the prism is scaled down more than the gratings, reflecting the goal of studying the galaxy spectra in more detail. Exposure times are listed in Table 5. The original plan was 8665 s in each of the five dispersion modes. However, small on-orbit changes in the timing model for parallel observations caused us to make small adjustments in the exposure times to be more efficient with the NIRCam parallels and fit into the program allocation.

As with Deep, the observing uses three-point nods with three shutter slits at each of three subpointing locations, for a total of 9 pixel dither locations. Each of these exposures is a single integration, using NRSIRS2 readout with 12 or 14 groups. As for the Deep pointings, some targets can only be placed on one or two subpointings, resulting in proportionally lower exposure time.

Four of the 12 Medium/JWST pointings are placed in GOODS-N and eight are in GOODS-S, which has wider JADES NIRCam imaging. Three of the GOODS-N pointings were observed between 2023 April 30 and May 5, at V3 P.A. $150\overset{\circ}{.}48$, covering a large fraction of the NIRCam Medium Prime mosaic. The fourth was delayed by an observatory failure to acquire guide stars and was observed at V3 P.A. $132\overset{\circ}{.}93$ on 2023 May 27.

Unfortunately, this final JWST/Medium observation in GOODS-N was affected by a short circuit in the NIRSpec MSA for some configurations, which, when triggered, produced a glow of light that flooded the detectors, ruining the NIRSpec data (T. D. Rawle et al. 2022). Half of the configurations were affected by these shorts (two of three prism and one of three grating). The other three configurations did not address the susceptible column of the MSA and, therefore, did not have the glow. We reobserved the missing configurations in 2024 May. The NIRCam coordinated parallel imaging data show no impact of the short.

For GOODS-S, four pointings are in the NIRCam Deep Prime mosaic, with the other four on the Medium Prime mosaic. Most of the GOODS-S Medium/JWST was delayed until Cycle 2, save one pointing (observation 1) observed on 2023 January 12 and 13. Observation 5 was observed 2023 October 19, and the other six in 2023 December. Pointing locations were designed to maximize coverage of bright high-redshift galaxy candidates from the NIRCam data.

This part of JADES is an investment of 222 hr, 77 in GOODS-N and 145 in GOODS-S, resulting in 146 prime open-shutter hours, a utilization of 66%. As before, the line detection sensitivity as a function of wavelength is shown in Figure 9.

5.6. NIRSpec Medium/HST Spectroscopy

The final tier is the shallowest and results from "parallel" observations during 10 of the NIRCam Medium Prime fields, four in GOODS-N and six in GOODS-S. We remind the reader that our naming convention is following the instrument that is driving our science design; in all coordinated parallels including NIRSpec MOS, NIRSpec is formally the prime instrument. The HST name refers to the fact that in the survey design, the JWST imaging was not yet available, and hence, the targeting was from HST data. We describe explicitly the

few cases for which we could use JWST-based targets, due to interruptions in the program.

As the imaging program requires a large 7″ offset to step over the V2-parallel SW chip gap, we opt to split each parallel opportunity into two largely distinct sets of targets. Offsets of this size when combined with the NIRSpec astrometric distortion at the MSA plane would otherwise cause many targets to become poorly registered within their slits. Each pointing in the mosaic was given a small 1″ freedom of motion to optimize the slit centration of a few highest-priority targets.

For each of these 20 target sets, we use four dispersers, omitting the G395H higher-resolution grating. Exposure times are listed in Table 5. GOODS-S was observed first, and here we used NRSIRS2 readout with 17 groups for the prism and 14 groups for the gratings, each observed once at each of three nod locations. Based on the first tranche of data in GOODS-S, we replanned GOODS-N so that the prism was observed twice with 14 groups at each pointing, to increase the S/N.

As this program results from the parallels of a reasonably tightly packed imaging mosaic, these NIRSpec MOS fields overlap substantially. However, any given object in the footprint of a single MSA pointing will often be poorly centered in its possible shutter, leading to many targets being rejected due to the low expected throughput. Collisions of prism spectral traces block many other targets. Therefore, several returns to a given area can be supported without much duplication. We do allow our targets to be observed twice (and our highest-priority targets up to four times), if the slit registration is favorable.

Our observations of the GOODS-S portion of this mosaic (observations 25–30 of program 1180) were affected by two short circuits in the NIRSpec MSA, similar to those described in the previous section. Some configurations did not use these columns of the MSA and, therefore, did not have the glow. The NIRCam coordinated parallel imaging data was unaffected in most cases, but the first half of observations 25 and 30 suffer from a short so bright that the illumination even reached NIRCam, as described in Section 4.6.

Only four of the 12 target sets were successfully observed without a bright short glow, and even in these cases, there is some persistence that affects the prism exposure in a small portion of the image. These are MSA configurations 2, 4, 6, and 10, which are the second half of observations 25, 26, 27, and 29, respectively. For a fifth target set (configuration 5, the first half of observation 26), the grating exposures are unaffected but the prism exposures were flooded by the short. These were reobserved in 2023 October, completing this configuration.

One of the target sets was not observed due to an unrelated telescope issue (configuration 12, second half of observation 30). As the first half of observation 30 was badly affected by shorts, we performed a complete repeat of this pointing as observation 136 in 2023 October at the original position angle, but with the same target selection as Medium/JWST. We allowed a small translation from the original mosaic to optimize the MSA for high-priority targets.

The other five target sets were reobserved on 2023 January 27 and 28, without new NIRCam parallels. Because the new position angle was already going to require a complete replan, we opted to collect the five single-nod designs into two pointings with smaller dithers, akin to the Medium/JWST program. Observation 134 has two subpointings; observation 135 has three. For these, we use the same NIRCam-based target selection that was used for the observation 1 of Medium/JWST in GOODS-S.

5.7. Data Quality Caveats

The NIRSpec MOS observations have been processed by using a pipeline developed by the ESA NIRSpec Science Operations Team and the NIRSpec GTO Team. The major steps of the data processing are described in A. J. Bunker et al. (2024) and F. D'Eugenio et al. (2025), while a detailed description of the pipeline and its performance will be reported in a forthcoming paper (J. Scholtz 2026, in preparation). Here, we discuss the main issues encountered during the data processing and analysis phase.

As mentioned in the previous sections, program 1180 year 1 was affected by short circuits in the NIRSpec MSA that produced bright glows of artificial light, ruining most of the exposures. In particular, 76 out of 132 exposures are ruined by such a bright glow. The other exposures did not suffer from this problem, but we found some persistence for the prism exposures that contaminate the spectra of ∼10% targets in the MSA design. In some cases, the signal of the persistence is as high as the sky background emission.

By inspecting the count-rate maps before background subtraction, we noticed that some shutters dedicated to the targets did not open (T. D. Rawle et al. 2022). We excluded these temporarily failed shutters from the data processing workflow. In each pointing, we found, on average, that ∼1% of the targets in the MSA masks are affected by this issue. In most cases, only one of the three-slitlet shutters was unexpectedly closed, but there are the same targets in which two or even all three shutters did not open during the observations. In these cases, the noise of the final products increases as the total exposure time is reduced.

Although the target selection was optimized to adopt the three-point nod strategy for the background subtraction process, some background shutters were contaminated by either background or foreground source. We have thus exploited either HST or NIRCam images to identify automatically contaminated shutters and excluded them in the background subtraction steps of the pipeline. This increases the noise of the background subtraction image but avoids a possible oversubtraction of background emission that could alter the final spectra of the targets.

6. MIRI Observations

6.1. MIRI Deep Parallel

The NIRCam Deep Prime program creates very deep MIRI parallels in GOODS-S, totaling 43.1 hr of open-shutter time in each of the four fields. The fields overlap only slightly, so that the deep area is about 10 arcmin^2.

The fields were designed to overlap the NIRCam Medium Parallel mosaic, but it turned out that the NIRCam Deep/HST Parallel field substantially overlaps as well. This allows these MIRI images to provide a very deep look at the high-redshift Universe. We note that while the MIRI fields are not on the UDF itself, they do fall near the center of the Chandra Deep Field South.

We decided to focus this time to the study of rest-frame 1–2 μm imaging of galaxies at redshifts above 3. For this, we selected the F770W filter as the most promising compromise

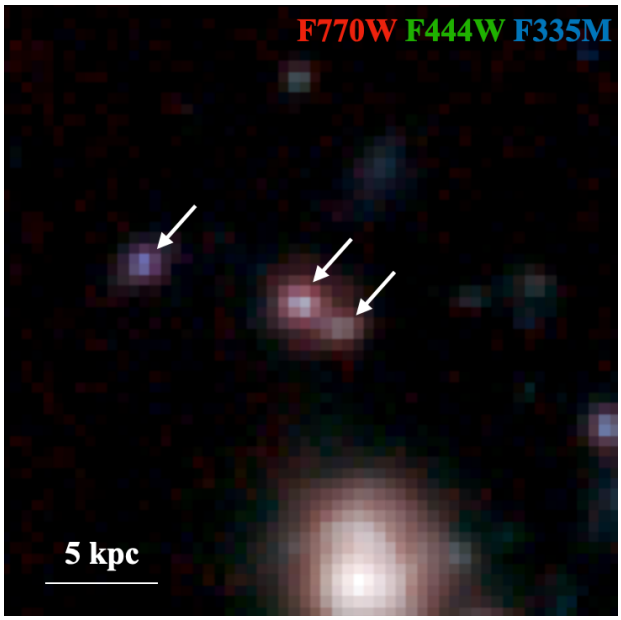

Figure 10. RGB (F770W, F444W, F335M) image of a trio of $z \sim 6$ photometric redshift candidates detected in the GOODS-S JADES Deep/MIRI parallel (24–25.6 AB with S/N $\sim$ 20–80 in F770W). All three are likely emission-line galaxies, with Hα in F444W. The leftmost candidate additionally has significant [O III]5007 emission in the F335M medium-band filter, resulting in a more purple color. The F770W probes the rest-frame 1 μm emission, a powerful constraint on the properties of older stellar populations.

between the rising background to the red and the lever arm relative to the deeper F410M and F444W data. An example of robust F770W detections of a trio of $z \sim 6$ photometric redshift candidates in the GOODS-S Deep/MIRI footprint can be seen in Figure 10. F770W is somewhat less sensitive in AB magnitude than F560W, but it more than doubles the logarithmic wavelength gap relative to 4.4 μm, allowing it to better detect power-law deviations in the slope of the near-IR SED. The longer band is also less likely to suffer from rest-optical emission-line contamination of the continuum light measurement; Hα falls in F560W at $6.6 < z < 8.4$, whereas F770W probes the rest-frame I band at these redshifts (J. M. Helton et al. 2025).

The MIRI data must, of course, follow the NIRCam exposure times and dither pattern. To keep the data volume within the allowed rate, we use SLOWR1 readout mode with 57 groups to yield a single integration of 1361 s per exposure. Each pointing then has 114 of these exposures, taken at 22 different dither points, for a total of 155.2 ks. Within each visit, the MIRI data is taken cycling through 9 or 4 subpixel dither locations. The resulting 10σ point-source sensitivity is 27.5 AB (Table 6).

6.2. MIRI Medium Parallel

In addition to the deep data, we conduct MIRI parallels with eight of the NIRCam Medium Prime pointings. Five of these are in GOODS-S and three in GOODS-N.

As these data are considerably shallower and yet have only mildly more area, we opt to focus on the science of intermediate-redshift galaxies ($z \sim 3$–5), where we can place strong constraints on the stellar emission SED, such as the regime of the contribution from TP-AGB stars, robustly identify the rising continuum associated with AGNs, and look for unusual SEDs. To accomplish these goals, we take moderately deep exposures in F770W and then use most of the time in the F1280W and F1500W filters, which gain in sensitivity over the Wide-field Infrared Survey Explorer W3 band by a factor of $\sim$1000. These filters present a notable increase in wavelength reach relative to F770W, while getting to sufficient depth to study intermediate-redshift galaxies. We could not use the reddest filters, as these would require the high-data-rate FAST readout. In GOODS-N, two-thirds of the MIRI pointings fall off of the planned NIRCam coverage, but are covered by CANDELS.

The layout in GOODS-S was originally designed to place the MIRI parallels largely on the Medium Prime NIRCam imaging. However, interruptions of the observing forced a replan, with only observations 20 and 24 falling at their original location. Observations 22, 219, and 223 are therefore rotated in P.A., placing their MIRI parallels northwest of the JADES Prime mosaic. The MIRI data from observations 219 and 223 substantially overlap NIRCam imaging from programs 1286, 1287, 2514, and 3990; those from observation 22 currently have no NIRCam coverage. In addition, because observation 20 was cut short, the two reobservation pointings (220 and 222) taken to replace the missing NIRCam filter have short F1500W MIRI imaging, again with a P.A. that places the MIRI field to the northwest. Only the data of 222 overlap current NIRCam data. The failed observation 23 also produces a small amount of F1500W imaging, not otherwise mentioned; future users of these exposures should be careful that the telescope may have been drifting without a guide star.

The exposure times are listed in Table 6. In all pointings, the dataset uses six dither locations. The dither locations have three close pairs with relatively long strides between them, and hence, there is a relatively large boundary region that has only two or four exposures. However, since MIRI is Nyquist sampled, this was considered acceptable. We always use the SLOWR1 readout, so as to reduce the data rate. F770W uses one integration per readout; F1280W and F1500W use two or three to avoid saturation on the background. In GOODS-S, where the available exposure times are longer, we observe F770W once per dither location and return to F1280W and F1500W two times each. In GOODS-N, our exposures are shorter, and we do not have any coverage from the Deep MIRI parallels; we therefore opt to include two exposures of F770W and two to three of F1280W per dither location.

6.3. Data Quality Caveats

The reduction of the MIRI data is described in S. Alberts et al. (2024). We have not encountered any substantial concerns with the MIRI data acquired, but note three minor issues. First, optimal background subtraction through the combination of multiple, spatially independent pointings requires the observations be taken in a short time interval due to the time-varying background. Some of the GS medium observations due to guide-star failures were reobserved outside of this time interval. This had a minor impact on the quality of the background subtraction. Second, we did find that the subpixel dither pattern used in the first Deep data, based on the F770W PSF size, was smaller than we would have preferred to use for the generation of sky flats. We find this can be mitigated by generating sky flats from roughly contemporaneous exposures over multiple pointings. Nevertheless, we have increased the dither steps in later observations. Last, astrometry corrections for MIRI pointings without overlapping

Table 6
Summary of MIRI Observations

Subsurvey	Number of Pointings	Area (arcmin^2)	Exposure Times (ks)			10σ AB Mag Limit		
			F770W	F1280W	F1500W	F770W	F1280W	F1500W
GOODS-S Deep	4	10	155	…	…	27.5	…	…
GOODS-S Medium Obs 24	1	3	5.6	10.9	13.5	25.6	24.6	24.2
GOODS-S Medium Obs 20	1	3	…	13.5	10.9	…	24.8	24.2
GOODS-S Medium Obs 220, 222	2	6	…	…	5.0	…	…	23.9
GOODS-S Medium Obs 22, 219, 223	3	9	5.0	10.9	10.9	25.6	24.7	24.3
GOODS-N Medium	3[a]	9	6.0	9.0	…	25.7	24.6	…

Notes. The number of pointings, area in arcmin^2, exposure times per filter, and the final AB magnitude detection threshold per filter for a 10σ point source. The aperture-corrected depths are estimated from the variance in blank-sky apertures of 0.″42, 0.″42, and 0.″49 diameter in F770W, F1280W, and F1500W, respectively, chosen to include 65% of the encircled energy. These are about 0.2 mag deeper than the JWST Exposure Time Calculator in F770W and 0.3 mag deeper in F1280W and F1500W. Only Obs 20 of the Medium/MIRI program overlaps the Deep/MIRI pointings; this observation omitted F770W to avoid redundancy. The mild overlap of Observation 222 and 223 as well as the mild overlap of two of the GOODS-N pointings has been ignored in the area computation.
[a] One of the GOODS-N pointings is mildly shallower, with 6.6 ks of exposure in F1280W.

NIRCam or HST coverage from CHARGE were done using matches to Gaia and have larger astrometric uncertainties due to the reliance on a small number of stars.

7. Preparing for JADES

Like many JWST observing programs, the JADES team engaged in substantial preparations for the dataset. We were particularly driven by the tight timescale, likely at most 6 weeks, to provide targets for multiobject spectroscopic follow-up from the NIRCam and MIRI imaging. This central goal of the program requires image reduction, mosaicking, source detection, source photometry, photometric redshift generation, target selection, and MSA design to be ready to run in quick order. We also sought to prepare for analysis of the spectroscopy, most obviously for the data reduction, extraction, and spectral analysis, as clearly the spectroscopic results would be desired to feed into the processing of the second field to be observed.

Part of this preparation was inherent in the needs of the instrument teams to support a wider range of commissioning and early science observations. Most obviously, we rely on the effort to develop exposure-level reduction software such as NCDhas written by K. Misselt and the pre-processing pipeline developed by the ESA NIRSpec Science Operations Team (S. M. Birkmann et al. 2022), which subsequently became the basis for the STScI stage 1 and 2 pipelines. To build and validate these tools pre-launch required creation of detailed codes to simulate instrument data: Guitarra[40] for NIRCam and the NIRSpec Instrument Performance Simulator (IPS; B. Dorner et al. 2016).

For NIRCam, we used Montage (J. C. Jacob et al. 2010) to combine the individual exposures into a mosaic. In order to identify outlier pixels (such as cosmic rays that have not been picked up by NCDhas), we first construct a median-based mosaic, which we then projected this median-based mosaic back to the individual exposures. We identified and masked outlier pixels that are 3σ outliers. In a final step, we constructed the mean-based mosaic and fully propagated the errors.

An important additional aspect of JADES preparation included optimizing our instrument configurations, integration times, and area to maximize our key science goals (e.g., lower panel of Figure 4). To this end, we developed JAdes extraGalactic Ultradeep Artificial Realizations, a novel phenomenological model of galaxy evolution out to $z \sim 15$ (JAGUAR; C. C. Williams et al. 2018),[41] incorporating known galaxy abundances, flux, color, and morphology relations across redshift. A key utility of JAGUAR includes both mock SEDs and full-resolution spectra, which we generated using BEAGLE (J. Chevallard & S. Charlot 2016) based on self-consistent models of stellar radiation and its transfer through the ISM and IGM. Beyond survey design, JAGUAR also enabled simulation of realistic galaxy fields using mock imaging tools like Guitarra, mock NIRSpec spectra, and optimizing our MSA design procedures.

With these tools, JADES then performed data challenges, simulating mock galaxy fields down to individual ramps and then reducing the data to make high-level products. For NIRCam, this included mosaicking, object detection, photometry, and photometric redshifting. For NIRSpec, mock target lists were used to build MSA designs with the eMPT code (N. Bonaventura et al. 2023), and simulated spectra (J. Chevallard et al. 2019) were run through reduction and extraction to develop tools for redshift and line-flux estimation (G. Giardino et al. 2019). A key advantage of these data challenges was to define data models for the interfaces between segments of the analysis. They also allowed us to generate test suites to validate each segment.

JADES conducted Data Challenge 1 (DC1) to initiate this process. The NIRCam component of DC1 concentrated on a single visit of Proposal 1180 (Observation 7, Visit 2), which is part of the NIRCam Deep Prime pointings. The DC1 simulations used nine ramps with seven DEEP8 groups for all filters used in the original JADES deep survey design (F090W, F115W, F150W, F200W, F277W, F356W, F410M, and F444W). The source catalog used for DC1 was derived solely from the JAGUAR mock catalog, where we assigned random positions in R.A. and decl. for the selected galaxies but in such a way as to maintain the same surface density of galaxies as the JAGUAR parent sample.

The NIRSpec component of DC1 was based on the NIRSpec Deep/JWST program. Note that 200 point-source

[40] https://github.com/cnaw/guitarra

[41] https://fenrir.as.arizona.edu/jwstmock

galaxies with realistic JAGUAR spectra were simulated in the prism and medium-resolution grating dispersers in each of the three Deep/JWST pointings. The data were processed with the NIRSpec IPS Pipeline Software (B. Dorner et al. 2016). The resulting output was simulated, flux-calibrated, with combined spectra for 370 galaxies, used to validate our choice of integration times for these faint targets (G. Giardino et al. 2019).

Following improvements in the code base, we then conducted Data Challenge 2 (DC2) as a set of more comprehensive exercises. DC2 covered about two-thirds of the area of the JADES survey in GOODS-S ($\sim$80 arcmin^2) and included Deep and Medium NIRCam pointings, using the same setup as the planned observations (e.g., exposure time, readout mode, dither positions) as recovered from the APT file. In contrast to DC1, the DC2 simulations included the field-of-view distortions, particularly important to test the ability to make astrometrically correct mosaics in sky coordinates and accounting for pixel subsampling when constructing these mosaics. Cosmic-ray hits were also added to the individual ramps. The DC2 sample used a combination of the CANDELS (N. A. Grogin et al. 2011; A. M. Koekemoer et al. 2011) catalog with Sérsic parameters estimated by A. van der Wel et al. (2012) and objects from JAGUAR, which also provides Sérsic parameters. The latter enabled including objects beyond the apparent magnitude limit and redshift cutoff of the HST data. In this process, we used the positions and shapes of all observed galaxies and supplemented these with mock galaxies where a fraction of the latter were included until the counts in apparent magnitudes and redshifts were as close as possible to the JAGUAR magnitude-redshift distribution. In addition to the galaxy catalog, we also created a separate set of images with stellar sources, which were used to verify the photometric calibration procedure. In both data challenges, a few objects with abnormal colors and Population III galaxies (E. Zackrisson et al. 2011) were added to test the efficacy of algorithms being tailored to detect outliers. For DC2, HST fluxes were also calculated (though no HST images created), which were used to estimate the number of low-redshift contaminants in the photometric redshift calculation. For the JAGUAR galaxies in DC2, noise was added to the mock HST fluxes, and uncertainties were estimated according to the depth of the available ancillary HST imaging.

For NIRSpec, these data challenges not only served to verify and practice ingesting NIRCam-generated and -formatted target catalogs and images into the NIRSpec target selection and MSA mask design work flow, but also provided a critical opportunity to augment the eMPT with needed features. In particular, we modified eMPT to be able to point the "prime" NIRSpec instrument such that the "secondary" NIRCam instrument achieved its intended elaborate mosaicking of the NIRCam Medium Prime fields described in Sections 4.2 and 5.6, while simultaneously exploiting the $\simeq 1''$ level permissible deviations from the nominal NIRCam pointing pattern to optimize the parallel NIRSpec exposures such that the largest possible number of the highest-priority HST targets were captured by the MSA. This task was further complicated by the peculiar manner in which the roll orientation of the NIRSpec MSA assigned to an observation by STScI does not refer to the center of the MSA, but rather to a reference point defined by median location of all targets contained in the NIRSpec input catalog entered into the APT (N. Bonaventura et al. 2023). Limiting the impact of this complication over the $6.'4$ lever arm between the field centers of the two instruments required an iterative approach in which the NIRSpec input catalog was gradually trimmed down to match the outer envelop of the final NIRSpec footprint.

The NIRSpec component of DC2 simulated an approximation of the GOODS-South Medium/HST tier. The NIRCam source scene described above was used to assign spectra and morphologies to the known HST prioritized target catalog. The eMPT was exercised to determine the optimum set of six pairs of pointing locations, within the small tolerance allowed given that in the real Medium/HST, a NIRCam mosaic would be made in parallel, which maximized the number of highest-priority targets assigned shutters. The eMPT was then run to assign targets to shutters in order of priority class. Spectra were simulated and processed in a similar manner to DC1. One difference is that contaminants that would fall within the target or background shutter were included in the simulation to assess the effects of contamination.

To manipulate these data challenges and to prepare for the real data, JADES also built visualization tools. To browse the sky, we developed FitsMap (R. Hausen & B. E. Robertson 2022), inspired in part by the Legacy Survey viewer led by D. Lang (A. Dey et al. 2019). FitsMap allows us to zoom and pan the sky, easily changing between image layers, with overlays from various catalogs that provide pop-up access to the database information. To study the SEDs and photometric redshift outputs, we developed JADESview,[42] which shows image thumbnails, photometric SEDs with best-fit template overlays, and photometric redshift likelihoods versus redshift.

We have found these preparations to be invaluable in handling the in-flight data. That said, unsurprisingly, the real data have presented additional challenges to which the team (and the community more broadly) must adjust. We have described some of these challenges here; others are described in our data release papers (D. J. Eisenstein et al. 2023; M. J. Rieke et al. 2023b; A. J. Bunker et al. 2024).

8. Conclusions

The JWST Advanced Deep Extragalactic Survey is bringing an ambitious deep imaging and spectroscopic infrared view of the GOODS-S and GOODS-N fields in the first cycle of JWST observing. With JADES, we use 545 hr of open-shutter dual-band NIRCam imaging and 240 open-shutter hours of MIRI imaging to cover about 210 arcmin^2 to very faint flux levels in 12 distinct bands. We then conduct extensive multiobject infrared spectroscopy using 339 open-shutter hours of NIRSpec MOS, observing over 5000 faint targets with both prism and grating dispersers.

The resulting JADES imaging and spectra provide an exquisite sample for the study of galaxy evolution. The dataset has yielded many candidates at redshifts above 8 (K. N. Hainline et al. 2024) and provided early spectroscopic confirmation galaxies at $z > 10$ (A. J. Bunker et al. 2023; E. Curtis-Lake et al. 2023; B. E. Robertson et al. 2023a; S. Tacchella et al. 2023; S. Carniani et al. 2024; J. Witstok et al. 2025). The amount of detail in both imaging and spectroscopy is very impressive and is revealing high-redshift galaxies to be a diverse set, with clear variations in morphology, emission-line ratios, and SFHs (e.g.,

[42] https://github.com/kevinhainline/JADESView

A. Dressler et al. 2023; R. Endsley et al. 2024; T. J. Looser et al. 2024). The spectra reveal the imprint of reionization through variations in Lyα emission (A. Saxena et al. 2023; J. Witstok et al. 2024) and signatures of the Gunn–Peterson damping wing (E. Curtis-Lake et al. 2023).

JADES also provides a useful design example for deep surveys, which we have documented in this paper. We have found great value in the medium-band F335M and F410M imaging and provide examples to achieve high pixel diversity in both imaging and spectroscopy. We have demonstrated how the multiplex of grating spectroscopy can be increased by allowing these spectra to overlap and using the shorter prism spectra to disambiguate emission lines. We are also confronting a number of challenges in carrying out the survey, such as recovering from lost data in a survey with substantial geometrical constraints and concerns with NIRCam persistence. We expect these will be useful learning experiences as the JWST mission matures.

As listed in Section 3.4, JADES is one of several extragalactic surveys being carried out in Cycle 1 of the JWST mission. These span a range of depth, areas, filter sets, and fields, and there is a productive complementarity in these choices. JADES is important because of its deep and reasonably wide coverage of the GOODS-S/HUDF and GOODS-N/HDF fields, where there is an awesome amount of multiwavelength imaging and spectroscopy, and because of its close coordination of JWST imaging and spectroscopy.

The first release of JADES data, focusing on year 1 Deep NIRCam imaging and NIRSpec multiobject spectroscopy on the HUDF, is presented in A. J. Bunker et al. (2024) and M. J. Rieke et al. (2023b). The second release, containing the initial data in the JADES Origins Field and the year 1 GOODS-S Medium Prime mosaic, is presented in D. J. Eisenstein et al. (2023). The third release (F. D'Eugenio et al. 2025) contains NIRSpec data taken before 2023 November, as well as the GOODS-N Prime imaging. All are available at https://archive.stsci.edu/hlsp/jades, doi:10.17909/8tdj-8n28, and the latest data can be viewed at http://jades.idies.jhu.edu/. Additional releases will follow in the coming year, and we post science updates from the survey at the JADES Collaboration website, https://jades-survey.github.io. JADES will provide the foundation for JWST's study of these two premier deep fields, and we look forward to many years of utilization and extension of this dataset.

Acknowledgments

The JADES Collaboration thanks the Instrument Development Teams and the instrument teams at the European Space Agency and the Space Telescope Science Institute for the support that made this program possible. We also thank our program coordinators at STScI for their help in planning complicated parallel observations.

This work is based in part on observations made with the NASA/ESA/CSA James Webb Space Telescope. The data were obtained from the Mikulski Archive for Space Telescopes at the Space Telescope Science Institute, which is operated by the Association of Universities for Research in Astronomy, Inc., under NASA contract NAS 5-03127 for JWST. These observations are associated with programs 1180, 1181, 1210, 1286, and 1287.

Processing for the JADES NIRCam data release was performed on the *lux* cluster at the University of California, Santa Cruz, funded by NSF MRI grant AST 1828315. This research makes use of ESA Datalabs (https://datalabs.esa.int/), an initiative by ESA's Data Science and Archives Division in the Science and Operations Department, Directorate of Science. This work was performed using resources provided by the Cambridge Service for Data Driven Discovery (CSD3) operated by the University of Cambridge Research Computing Service (www.csd3.cam.ac.uk), provided by Dell EMC and Intel using Tier-2 funding from the Engineering and Physical Sciences Research Council (capital grant EP/T022159/1), and DiRAC funding from the Science and Technology Facilities Council (www.dirac.ac.uk).

M.R., A.D., E.E., D.J.E., B.D.J., B.R., G.R., F.S., and C.N. A.W. acknowledge support from the NIRCam Science Team contract to the University of Arizona, NAS5-02105. D.J.E. is further supported as a Simons Investigator. S.Ar. acknowledges support from grant PID2021-127718NB-I00 funded by the Spanish Ministry of Science and Innovation/State Agency of Research (MICIN/AEI/10.13039/501100011033). S.Al. acknowledges support from the JWST Mid-Infrared Instrument (MIRI) Science Team Lead, grant 80NSSC18K0555, from NASA Goddard Space Flight Center to the University of Arizona. A.J.B., A.J.C., J.C., I.E.B.W., A.S., and G.C.J. acknowledge funding from the "FirstGalaxies" Advanced Grant from the European Research Council (ERC) under the European Union's Horizon 2020 research and innovation program (grant agreement No. 789056). E.C.L. acknowledges support of an STFC Webb Fellowship (ST/W001438/1). Funding for this research was provided by the Johns Hopkins University, Institute for Data Intensive Engineering and Science (IDIES). The Cosmic Dawn Center (DAWN) is funded by the Danish National Research Foundation under grant No. 140. R.M., W.M.B., F.D.E., T.J.L., J.S., L.S., and J. W. acknowledge support by the Science and Technology Facilities Council (STFC) and by the ERC through Advanced grant 695671 "QUENCH." R.M. also acknowledges funding from a research professorship from the Royal Society. J.W. further acknowledges support from the Fondation MERAC. The research of C.C.W. is supported by NOIRLab, which is managed by the Association of Universities for Research in Astronomy (AURA) under a cooperative agreement with the National Science Foundation. A.L.D. thanks the University of Cambridge Harding Distinguished Postgraduate Scholars Programme and Technology Facilities Council (STFC) Center for Doctoral Training (CDT) in Data intensive science at the University of Cambridge (STFC grant No. 2742605) for a PhD studentship. B.R.D.P. acknowledges support from the research project PID2021-127718NB-I00 of the Spanish Ministry of Science and Innovation/State Agency of Research (MICIN/AEI/ 10.13039/501100011033). R.S. acknowledges support from an STFC Ernest Rutherford Fellowship (ST/S004831/1). C.Wo. is supported by the National Science Foundation through the Graduate Research Fellowship Program funded by grant award No. DGE-1746060. D.P. acknowledges support by the Huo Family Foundation through a P.C. Ho PhD Studentship. H.Ü. gratefully acknowledges support by the Isaac Newton Trust and by the Kavli Foundation through a Newton-Kavli Junior Fellowship. L.W. acknowledges support from the National Science Foundation Graduate Research Fellowship under grant No. DGE-2137419. M.P. acknowledges support from the research project PID2021-127718NB-I00 of the Spanish Ministry of Science and Innovation/State Agency of

Research (MICIN/AEI/10.13039/501100011033), and the Programa Atracción de Talento de la Comunidad de Madrid via grant 2018-T2/TIC-11715. M.S.S. acknowledges support by the Science and Technology Facilities Council (STFC) grant ST/V506709/1. R.E.H. acknowledges support from the National Science Foundation Graduate Research Fellowship Program under grant No. DGE-1746060. S.Ca. acknowledges support by European Union's HE ERC Starting grant No. 101040227—WINGS. The research of K.B. is supported in part by the Australian Research Council Centre of Excellence for All Sky Astrophysics in 3 Dimensions (ASTRO 3D), through project No. CE170100013. Support for program JWST-GO-1963 was provided in part by NASA through a grant from the Space Telescope Science Institute, which is operated by the Associations of Universities for Research in Astronomy, Incorporated, under NASA contract NAS 5-26555.

Software: Aladin Sky Atlas (F. Bonnarel et al. 2000, http://aladin.u-strasbg.fr/); Astronomer's Proposal Tools (https://www.stsci.edu/scientific-community/software/astronomers-proposal-tool-apt); BEAGLE (J. Chevallard & S. Charlot 2016); eMPT code (N. Bonaventura et al. 2023); FitsMap (R. Hausen & B. E. Robertson 2022); Guitarra (https://github.com/cnaw/guitarra); grizli (G. Brammer 2023); JADESview (https://github.com/kevinhainline/JADESView); Montage (J. C. Jacob et al. 2010); NCDhas (K. Misselt 2025, private communication); NIRSpec Instrument Performance Simulator (B. Dorner et al. 2016).

ORCID iDs

Daniel J. Eisenstein https://orcid.org/0000-0002-2929-3121
Chris Willott https://orcid.org/0000-0002-4201-7367
Stacey Alberts https://orcid.org/0000-0002-8909-8782
Santiago Arribas https://orcid.org/0000-0001-7997-1640
Nina Bonaventura https://orcid.org/0000-0001-8470-7094
Andrew J. Bunker https://orcid.org/0000-0002-8651-9879
Alex J. Cameron https://orcid.org/0000-0002-0450-7306
Stefano Carniani https://orcid.org/0000-0002-6719-380X
Stephane Charlot https://orcid.org/0000-0003-3458-2275
Emma Curtis-Lake https://orcid.org/0000-0002-9551-0534
Francesco D'Eugenio https://orcid.org/0000-0003-2388-8172
Pierre Ferruit https://orcid.org/0000-0001-8895-0606
Giovanna Giardino https://orcid.org/0000-0002-9262-7155
Kevin Hainline https://orcid.org/0000-0003-4565-8239
Ryan Hausen https://orcid.org/0000-0002-8543-761X
Peter Jakobsen https://orcid.org/0000-0002-6780-2441
Benjamin D. Johnson https://orcid.org/0000-0002-9280-7594
Roberto Maiolino https://orcid.org/0000-0002-4985-3819
Bernard J. Rauscher https://orcid.org/0000-0003-2662-6821
Marcia Rieke https://orcid.org/0000-0002-7893-6170
George Rieke https://orcid.org/0000-0003-2303-6519
Hans-Walter Rix https://orcid.org/0000-0003-4996-9069
Brant Robertson https://orcid.org/0000-0002-4271-0364
Daniel P. Stark https://orcid.org/0000-0001-6106-5172
Sandro Tacchella https://orcid.org/0000-0002-8224-4505
Christina C. Williams https://orcid.org/0000-0003-2919-7495
Christopher N. A. Willmer https://orcid.org/0000-0001-9262-9997
William M. Baker https://orcid.org/0000-0003-0215-1104
Stefi Baum https://orcid.org/0000-0002-4735-8224
Rachana Bhatawdekar https://orcid.org/0000-0003-0883-2226
Kristan Boyett https://orcid.org/0000-0003-4109-304X
Zuyi Chen https://orcid.org/0000-0002-2178-5471
Jacopo Chevallard https://orcid.org/0000-0002-7636-0534
Chiara Circosta https://orcid.org/0000-0001-8522-9434
Mirko Curti https://orcid.org/0000-0002-2678-2560
A. Lola Danhaive https://orcid.org/0000-0002-9708-9958
Christa DeCoursey https://orcid.org/0000-0002-4781-9078
Ryan Endsley https://orcid.org/0000-0003-4564-2771
Anna de Graaff https://orcid.org/0000-0002-2380-9801
Alan Dressler https://orcid.org/0000-0002-6317-0037
Eiichi Egami https://orcid.org/0000-0003-1344-9475
Jakob M. Helton https://orcid.org/0000-0003-4337-6211
Raphael E. Hviding https://orcid.org/0000-0002-4684-9005
Zhiyuan Ji https://orcid.org/0000-0001-7673-2257
Gareth C. Jones https://orcid.org/0000-0002-0267-9024
Nimisha Kumari https://orcid.org/0000-0002-5320-2568
Nora Lützgendorf https://orcid.org/0000-0002-4034-0080
Isaac Laseter https://orcid.org/0000-0003-4323-0597
Tobias J. Looser https://orcid.org/0000-0002-3642-2446
Jianwei Lyu https://orcid.org/0000-0002-6221-1829
Michael V. Maseda https://orcid.org/0000-0003-0695-4414
Erica Nelson https://orcid.org/0000-0002-7524-374X
Eleonora Parlanti https://orcid.org/0000-0002-7392-7814
Michele Perna https://orcid.org/0000-0002-0362-5941
Dávid Puskás https://orcid.org/0000-0001-8630-2031
Tim Rawle https://orcid.org/0000-0002-7028-5588
Bruno Rodríguez Del Pino https://orcid.org/0000-0001-5171-3930
Wiphu Rujopakarn https://orcid.org/0000-0002-0303-499X
Lester Sandles https://orcid.org/0000-0001-9276-7062
Aayush Saxena https://orcid.org/0000-0001-5333-9970
Katherine Sharpe https://orcid.org/0000-0001-8225-8969
Irene Shivaei https://orcid.org/0000-0003-4702-7561
Maddie S. Silcock https://orcid.org/0009-0002-0651-5761
Charlotte Simmonds https://orcid.org/0000-0003-4770-7516
Maya Skarbinski https://orcid.org/0009-0004-0844-0657
Renske Smit https://orcid.org/0000-0001-8034-7802
Meredith Stone https://orcid.org/0000-0002-9720-3255
Katherine A. Suess https://orcid.org/0000-0002-1714-1905
Fengwu Sun https://orcid.org/0000-0002-4622-6617
Mengtao Tang https://orcid.org/0000-0001-5940-338X
Michael W. Topping https://orcid.org/0000-0001-8426-1141
Hannah Übler https://orcid.org/0000-0003-4891-0794
Natalia C. Villanueva https://orcid.org/0000-0001-6917-4656
Imaan E. B. Wallace https://orcid.org/0000-0002-0695-8485
Lily Whitler https://orcid.org/0000-0003-1432-7744
Joris Witstok https://orcid.org/0000-0002-7595-121X
Charity Woodrum https://orcid.org/0000-0001-5962-7260

References

Akins, H. B., Casey, C. M., Allen, N., et al. 2023, ApJ, 956, 61
Alberts, S., Lyu, J., Shivaei, I., et al. 2024, ApJ, 976, 224
Alberts, S., & Noble, A. 2022, Univ, 8, 554
Alberts, S., Rujopakarn, W., Rieke, G. H., Jagannathan, P., & Nyland, K. 2020, ApJ, 901, 168
Algera, H. S. B., Inami, H., Oesch, P. A., et al. 2023, MNRAS, 518, 6142
Arrabal Haro, P., Dickinson, M., Finkelstein, S. L., et al. 2023, Natur, 622, 707
Bagley, M. B., Finkelstein, S. L., Koekemoer, A. M., et al. 2023, ApJL, 946, L12
Baker, W. M., Tacchella, S., Johnson, B. D., et al. 2025, NatAs, 9, 141
Barrufet, L., Oesch, P. A., Marques-Chaves, R., et al. 2025, MNRAS, 537, 3453
Barrufet, L., Oesch, P. A., Weibel, A., et al. 2023, MNRAS, 522, 449
Beckwith, S. V. W., Stiavelli, M., Koekemoer, A. M., et al. 2006, AJ, 132, 1729
Birkmann, S. M., Giardino, G., Sirianni, M., et al. 2022, SPIE, 12180, 121802P
Böker, T., Beck, T. L., Birkmann, S. M., et al. 2023, PASP, 135, 038001
Bonaventura, N., Jakobsen, P., Ferruit, P., Arribas, S., & Giardino, G. 2023, A&A, 672, A40
Bonnarel, F., Fernique, P., Bienaymé, O., et al. 2000, A&AS, 143, 33
Bouwens, R., Illingworth, G., Oesch, P., et al. 2023, MNRAS, 523, 1009
Bouwens, R. J., Illingworth, G. D., Oesch, P. A., et al. 2010, ApJL, 709, L133
Brammer, G. 2023, grizli, v1.8.10, Zenodo, doi:10.5281/ZENODO.7963066
Bunker, A. J., Cameron, A. J., Curtis-Lake, E., et al. 2024, A&A, 690, A288
Bunker, A. J., Saxena, A., Cameron, A. J., et al. 2023, A&A, 677, A88
Cameron, A. J., Saxena, A., Bunker, A. J., et al. 2023, A&A, 677, A115
Carnall, A. C., McLeod, D. J., McLure, R. J., et al. 2023, MNRAS, 520, 3974
Carniani, S., Hainline, K., D'Eugenio, F., et al. 2024, Natur, 633, 318
Chevallard, J., & Charlot, S. 2016, MNRAS, 462, 1415
Chevallard, J., Curtis-Lake, E., Charlot, S., et al. 2019, MNRAS, 483, 2621
Coe, D., Zitrin, A., Carrasco, M., et al. 2013, ApJ, 762, 32
Curti, M., D'Eugenio, F., Carniani, S., et al. 2023, MNRAS, 518, 425
Curtis-Lake, E., Carniani, S., Cameron, A., et al. 2023, NatAs, 7, 622
DeCoursey, C., Egami, E., Pierel, J. D. R., et al. 2025, ApJ, 979, 250
de Graaff, A., Rix, H.-W., Carniani, S., et al. 2024, A&A, 684, A87
D'Eugenio, F., Cameron, A. J., Scholtz, J., et al. 2025, ApJS, 277, 4
Dey, A., Schlegel, D. J., Lang, D., et al. 2019, AJ, 157, 168
Donnan, C. T., McLeod, D. J., Dunlop, J. S., et al. 2023, MNRAS, 518, 6011
Dorner, B., Giardino, G., Ferruit, P., et al. 2016, A&A, 592, A113
Doyon, R., Hutchings, J., Willott, C., et al. 2023, PASP, 135, 098001
Dressler, A., Vulcani, B., Treu, T., et al. 2023, ApJL, 947, L27
Dunlop, J. S., McLure, R. J., Biggs, A. D., et al. 2017, MNRAS, 466, 861
Eisenstein, D. J., Johnson, B. D., Robertson, B., et al. 2025, ApJS, 281, 50
Ellis, R. S., McLure, R. J., Dunlop, J. S., et al. 2013, ApJL, 763, L7
Endsley, R., Stark, D. P., Whitler, L., et al. 2023, MNRAS, 524, 2312
Endsley, R., Stark, D. P., Whitler, L., et al. 2024, MNRAS, 533, 1111
Fan, X., Bañados, E., & Simcoe, R. A. 2023, ARA&A, 61, 373
Ferguson, H. C., Dickinson, M., & Williams, R. 2000, ARA&A, 38, 667
Ferreira, L., Adams, N., Conselice, C. J., et al. 2022, ApJL, 938, L2
Ferreira, L., Conselice, C. J., Sazonova, E., et al. 2023, ApJ, 955, 94
Ferruit, P., Jakobsen, P., Giardino, G., et al. 2022, A&A, 661, A81
Fontana, A., Vanzella, E., Pentericci, L., et al. 2010, ApJL, 725, L205
Franco, M., Elbaz, D., Béthermin, M., et al. 2018, A&A, 620, A152
Fudamoto, Y., Oesch, P. A., Schouws, S., et al. 2021, Natur, 597, 489
Fujimoto, S., Finkelstein, S. L., Burgarella, D., et al. 2023, ApJ, 955, 130
Furtak, L. J., Zitrin, A., Plat, A., et al. 2023, ApJ, 952, 142
Gaia Collaboration, Brown, A. G. A., Vallenari, A., et al. 2018, A&A, 616, A1
Gaia Collaboration, Prusti, T., de Bruijne, J., H., J., et al. 2016, A&A, 595, A1
Gardner, J. P., Mather, J. C., Abbott, R., et al. 2023, PASP, 135, 068001
Giacconi, R., Zirm, A., Wang, J., et al. 2002, ApJS, 139, 369
Giardino, G., Ferruit, P., & Chevallard, J. 2019, ASPC, 523, 645
Giavalisco, M., Ferguson, H. C., Koekemoer, A. M., et al. 2004, ApJL, 600, L93
Gómez-Guijarro, C., Magnelli, B., Elbaz, D., et al. 2023, A&A, 677, A34
Grogin, N. A., Kocevski, D. D., Faber, S. M., et al. 2011, ApJS, 197, 35
Hainline, K. N., Johnson, B. D., Robertson, B., et al. 2024, ApJ, 964, 71
Harikane, Y., Zhang, Y., Nakajima, K., et al. 2023, ApJ, 959, 39
Hatsukade, B., Kohno, K., Yamaguchi, Y., et al. 2018, PASJ, 70, 105
Hausen, R., & Robertson, B. E. 2022, A&C, 39, 100586
Helton, J. M., Alberts, S., Rieke, G. H., et al. 2025, arXiv:2506.02099
Helton, J. M., Sun, F., Woodrum, C., et al. 2024, ApJ, 962, 124
Hsiao, T. Y.-Y., Abdurro'uf, Coe, D., et al. 2024, ApJ, 973, 8
Huertas-Company, M., Iyer, K. G., Angeloudi, E., et al. 2024, A&A, 685, A48
Illingworth, G., Magee, D., Bouwens, R., et al. 2016, arXiv:1606.00841
Illingworth, G. D., Magee, D., Oesch, P. A., et al. 2013, ApJS, 209, 6
Jacob, J. C., Katz, D. S., Berriman, G. B., et al., 2010 Montage: An Astronomical Image Mosaicking Toolkit, Astrophysics Source Code Library, ascl:1010.036
Jacobs, C., Glazebrook, K., Calabrò, A., et al. 2023, ApJL, 948, L13
Jakobsen, P., Ferruit, P., Alves de Oliveira, C., et al. 2022, A&A, 661, A80
Ji, Z., Williams, C. C., Tacchella, S., et al. 2024, ApJ, 974, 135
Jones, G. C., Bunker, A. J., Saxena, A., et al. 2024, A&A, 683, A238
Jung, I., Finkelstein, S. L., Arrabal Haro, P., et al. 2024, ApJ, 967, 73
Kartaltepe, J. S., Rose, C., Vanderhoof, B. N., et al. 2023, ApJL, 946, L15
Kashino, D., Lilly, S. J., Matthee, J., et al. 2023, ApJ, 950, 66
Kocevski, D. D., Onoue, M., Inayoshi, K., et al. 2023, ApJL, 954, L4
Koekemoer, A. M., Faber, S. M., Ferguson, H. C., et al. 2011, ApJS, 197, 36
Kokorev, V., Brammer, G., Fujimoto, S., et al. 2022, ApJS, 263, 38
Labbé, I., van Dokkum, P., Nelson, E., et al. 2023, Natur, 616, 266
Larson, R. L., Finkelstein, S. L., Kocevski, D. D., et al. 2023, ApJL, 953, L29
Looser, T. J., D'Eugenio, F., Maiolino, R., et al. 2024, Natur, 629, 53
Lu, T.-Y., Mason, C. A., Hutter, A., et al. 2024, MNRAS, 528, 4872
Luo, B., Bauer, F. E., Brandt, W. N., et al. 2008, ApJS, 179, 19
Magnelli, B., Gómez-Guijarro, C., Elbaz, D., et al. 2023, A&A, 678, A83
Maiolino, R., Scholtz, J., Curtis-Lake, E., et al. 2024a, A&A, 691, A145
Maiolino, R., Scholtz, J., Witstok, J., et al. 2024b, Natur, 627, 59
Mascia, S., Pentericci, L., Calabrò, A., et al. 2023, A&A, 672, A155
Mason, C. A., Treu, T., Dijkstra, M., et al. 2018, ApJ, 856, 2
Matthee, J., Mackenzie, R., Simcoe, R. A., et al. 2023, ApJ, 950, 67
Matthee, J., Naidu, R. P., Brammer, G., et al. 2024, ApJ, 963, 129
McKinney, J., Manning, S. M., Cooper, O. R., et al. 2023, ApJ, 956, 72
Morishita, T., Mason, C. A., Kreilgaard, K. C., et al. 2025, ApJ, 983, 152
Morishita, T., Roberts-Borsani, G., Treu, T., et al. 2023, ApJL, 947, L24
Nakajima, K., Ouchi, M., Isobe, Y., et al. 2023, ApJS, 269, 33
Nanayakkara, T., Glazebrook, K., Jacobs, C., et al. 2024, NatSR, 14, 3724
Nelson, E. J., Suess, K. A., Bezanson, R., et al. 2023, ApJL, 948, L18
Oesch, P. A., Brammer, G., Naidu, R. P., et al. 2023, MNRAS, 525, 2864
Oesch, P. A., Brammer, G., van Dokkum, P. G., et al. 2016, ApJ, 819, 129
Östlin, G., Pérez-González, P. G., Melinder, J., et al. 2025, A&A, 696, A57
Ouchi, M., Ono, Y., & Shibuya, T. 2020, ARA&A, 58, 617
Pentericci, L., Vanzella, E., Fontana, A., et al. 2014, ApJ, 793, 113
Pérez-González, P. G., Barro, G., Annunziatella, M., et al. 2023, ApJL, 946, L16
Pérez-González, P. G., Rinaldi, P., Caputi, K. I., et al. 2024, ApJL, 969, L10
Planck Collaboration, Aghanim, N., Akrami, Y., et al. 2020, A&A, 641, A6
Rawle, T. D., Giardino, G., Franz, D. E., et al. 2022, SPIE, 12180, 121803R
Reddy, N. A., Topping, M. W., Sanders, R. L., Shapley, A. E., & Brammer, G. 2023a, ApJ, 952, 167
Reddy, N. A., Topping, M. W., Sanders, R. L., Shapley, A. E., & Brammer, G. 2023b, ApJ, 948, 83
Rieke, M. J., Kelly, D. M., Misselt, K., et al. 2023a, PASP, 135, 028001
Rieke, M. J., Robertson, B., Tacchella, S., et al. 2023b, ApJS, 269, 16
Rigby, J., Perrin, M., McElwain, M., et al. 2023, PASP, 135, 048001
Robertson, B. E. 2022, ARA&A, 60, 121
Robertson, B. E., Tacchella, S., Johnson, B. D., et al. 2023a, NatAs, 7, 611
Robertson, B. E., Tacchella, S., Johnson, B. D., et al. 2023b, ApJL, 942, L42
Rujopakarn, W., Dunlop, J. S., Rieke, G. H., et al. 2016, ApJ, 833, 12
Sanders, R. L., Shapley, A. E., Topping, M. W., Reddy, N. A., & Brammer, G. B. 2023, ApJ, 955, 54
Sandles, L., D'Eugenio, F., Maiolino, R., et al. 2024, A&A, 691, A305
Saxena, A., Robertson, B. E., Bunker, A. J., et al. 2023, A&A, 678, A68
Scholtz, J., Maiolino, R., D'Eugenio, F., et al. 2025, A&A, 697, A175
Shapley, A. E., Sanders, R. L., Reddy, N. A., Topping, M. W., & Brammer, G. B. 2023, ApJ, 954, 157
Simmonds, C., Tacchella, S., Maseda, M., et al. 2023, MNRAS, 523, 5468
Stark, D. P., Ellis, R. S., Chiu, K., Ouchi, M., & Bunker, A. 2010, MNRAS, 408, 1628
Steinhardt, C. L., Jespersen, C. K., & Linzer, N. B. 2021, ApJ, 923, 8
Strait, V., Brammer, G., Muzzin, A., et al. 2023, ApJL, 949, L23
Suess, K. A., Bezanson, R., Nelson, E. J., et al. 2022, ApJL, 937, L33
Sun, F., Helton, J. M., Egami, E., et al. 2024, ApJ, 961, 69
Tacchella, S., Eisenstein, D. J., Hainline, K., et al. 2023, ApJ, 952, 74
Tang, M., Stark, D. P., Chen, Z., et al. 2023, MNRAS, 526, 1657
van der Wel, A., Bell, E. F., Häussler, B., et al. 2012, ApJS, 203, 24
Walter, F., Decarli, R., Aravena, M., et al. 2016, ApJ, 833, 67
Whitaker, K. E., Ashas, M., Illingworth, G., et al. 2019, ApJS, 244, 16
Whitler, L., Endsley, R., Stark, D. P., et al. 2023, MNRAS, 519, 157
Whitler, L., Stark, D. P., Endsley, R., et al. 2024, MNRAS, 529, 855
Williams, C. C., Curtis-Lake, E., Hainline, K. N., et al. 2018, ApJS, 236, 33

Williams, C. C., Labbe, I., Spilker, J., et al. 2019, ApJ, 884, 154
Williams, C. C., Oesch, P. A., Weibel, A., et al. 2025, ApJ, 979, 140
Williams, C. C., Tacchella, S., Maseda, M. V., et al. 2023, ApJS, 268, 64
Williams, R. E., Blacker, B., Dickinson, M., et al. 1996, AJ, 112, 1335
Withers, S., Muzzin, A., Ravindranath, S., et al. 2023, ApJL, 958, L14
Witstok, J., Jakobsen, P., Maiolino, R., et al. 2025, Natur, 639, 897
Witstok, J., Shivaei, I., Smit, R., et al. 2023, Natur, 621, 267
Witstok, J., Smit, R., Saxena, A., et al. 2024, A&A, 682, A40
Wright, G. S., Rieke, G. H., Glasse, A., et al. 2023, PASP, 135, 048003
Zackrisson, E., Rydberg, C.-E., Schaerer, D., Östlin, G., & Tuli, M. 2011, ApJ, 740, 13
Zavala, J. A., Buat, V., Casey, C. M., et al. 2023, ApJL, 943, L9